Impacts of Cumulus Convection and Turbulence Parameterizations on the Convection-Permitting Simulation of Typhoon Precipitation

XIAOMING SHI[a] AND YUEYA WANG[a]

[a] *Division of Environment and Sustainability, Hong Kong University of Science and Technology, Hong Kong, China*

(Manuscript received 6 February 2022, in final form 20 July 2022)

ABSTRACT: Convection-permitting resolutions, which refer to kilometer-scale horizontal grid spacings, have become increasingly popular in regional numerical weather prediction and climate studies. However, this resolution range is in the gray zone for the simulation of convection, where conventional cumulus convection and subgrid-scale (SGS) turbulence parameterizations are inadequate for such grid spacings due to invalid assumptions and simplifications. Recent studies demonstrated that the magnitudes of SGS fluxes of momentum and scalars are comparable to those of resolved fluxes at convection-permitting resolutions and that horizontal SGS components are as important as the vertical SGS component. Thus, it appears necessary to adapt available schemes to model the SGS effects of convective motions for the gray zone. Here, we investigated the efficacy of separately parameterizing the vertical and horizontal SGS effects in improving the convection-permitting simulation of Typhoon Vicente (2012). To represent the vertical SGS turbulence effect, we evaluated the Grell-3, Tiedtke, and multiscale Kain–Fritsch (MSKF) schemes in the Weather Research and Forecasting (WRF) Model; the MSKF scheme is scale adaptive, whereas the other two are conventional cumulus schemes. For horizontal SGS turbulence, we evaluated the effects of the traditional Smagorinsky scheme and our newly developed reconstruction and nonlinear anisotropy (RNA) model, which models not only downgradient diffusion but also backscatter. We found that the simulation combining the MSKF and RNA schemes exhibits the best skill in predicting precipitation, especially rainfall extremes. The advantages are rooted in the MSKF scheme's scale-awareness and parameterized cloud–radiation feedback and in the backscatter-enabling capability of the RNA model.

SIGNIFICANCE STATEMENT: Operational numerical weather prediction and some climate simulations have approached kilometer-scale horizontal resolutions, called convection-permitting resolutions. However, details of convective storms are not well represented at these resolutions, and small-scale fluid motions can potentially impact the overall simulation performance. In practice, the effects of such unresolved turbulent eddies were once neglected. We suggest representing these effects in the vertical and horizontal directions with an adaptive cumulus convection parameterization and an advanced turbulence model, respectively, which significantly improve the simulation of tropical cyclones. This framework allows us to adapt convection schemes developed by the mesoscale modeling community and turbulence schemes studied by large-eddy simulation groups for representing three-dimensional turbulence in the convection-permitting regime.

KEYWORDS: Convection; Turbulence; Tropical cyclones; Numerical weather prediction/forecasting; Subgrid-scale processes

1. Introduction

Advances in computing capabilities have allowed numerical weather predictions and climate simulations to be performed at kilometer-scale resolution for some regions around the world (Seity et al. 2011; Raynaud and Bouttier 2017; Porson et al. 2020; Liu et al. 2017). Despite such significant improvements in the quantitative predictions of weather and climate attributable to these resolution refinements, critical challenges remain in numerical simulations at such grid spacings, referred to as convection-permitting resolutions (Kendon et al. 2021; Zhang et al. 2021a), primarily because these resolutions are in the gray zone for many subgrid-scale (SGS) processes, including turbulence, convection, and land surface fluxes (Honnert et al. 2020; Shi et al. 2019; Kendon et al. 2021).

The concept of a gray zone in numerical simulations originates from the term "terra incognita" coined by Wyngaard (2004), who used the term to describe the difficulties in parameterizing turbulence when the grid spacing is neither sufficiently fine to fully resolve energetic eddies, as in a large-eddy simulation (LES), nor sufficiently large to model turbulence entirely on the SGS, as in conventional mesoscale and global models. The physical assumptions of conventional LES- or mesoscale-type turbulence parameterizations tend to break down in terra incognita, rendering them inappropriate for modeling turbulence. More recently, terra incognita has typically been referred to as the numerical gray zone (e.g., Zhou et al. 2014; Boutle et al. 2014). Chow et al. (2019) generalized the concept of the gray zone as the challenges encountered when transitioning from parameterized physical processes to the explicit resolving of those processes as the model resolution is refined.

Tropical cyclones have severe socioeconomic impacts; hence, accurate predictions of such events can substantially benefit

Corresponding author: Xiaoming Shi, shixm@ust.hk

DOI: 10.1175/MWR-D-22-0057.1

society. However, the representations of convection and turbulence, among other factors, can significantly influence the numerical predictions of tropical cyclones at convection-permitting resolutions due to gray-zone challenges. At the early stage of tropical cyclogenesis, deep cumulonimbus convection with strong vorticity, which manifests as a phenomenon called a vortical hot tower, is a crucial mechanism by which energy and vorticity are added to the developing cyclone (Hendricks et al. 2004). For mature tropical cyclones, the eyewall cloud is characterized by slantwise convective motion that (to the leading order) maintains a state of nearly conditional symmetric neutrality and on which intermittently occurring buoyant convective cells are superimposed; at the same time, distant rainbands represent mainly organized ordinary deep convection relatively unconstrained by the inner-core vortex of the cyclone (Houze 2014). The kilometer-scale resolution is indeed within the gray zone for the simulation of deep convection (Shi et al. 2019), but conventional cumulus parameterizations are theoretically valid only for coarse grids and thus are usually not recommended for resolutions of $\lesssim$4 km (Skamarock et al. 2019).

The recent development of scale-aware cumulus parameterization schemes (Grell and Freitas 2014; Zheng et al. 2016) offers a promising solution to the gray-zone representation of partially SGS convection. The resolution dependence of these scale-aware schemes ensures a smooth transition from fully parameterized convection to fully explicit convection as the resolution is refined. Test cases with grid spacing $\geq$ 4 km suggest that such scale-aware cumulus parameterizations can significantly improve the precipitation prediction in convection-permitting simulations (Mahoney 2016; Gao et al. 2017). Therefore, this study aims to evaluate the efficacy of a scale-aware cumulus parameterization in improving the convection-permitting simulation of tropical cyclone precipitation.

Another gray-zone challenge confronted in the simulation of tropical cyclones is the representation of SGS turbulence. Some previous studies estimated that for boundary layer turbulence, the threshold resolution of the gray zone is $\mathcal{O}(100)$ m (Shi et al. 2018; Honnert et al. 2020). Thus, convection-permitting resolutions are marginally within the gray zone, and conventional planetary boundary layer (PBL) turbulence schemes might still be theoretically valid. However, neither conventional PBL schemes nor cumulus parameterizations consider the effect of SGS turbulence in the horizontal directions, which are ignored because the environment is assumed to be horizontally homogeneous at SGSs. Nevertheless, previous studies found that simulations of convective storms are highly sensitive to the horizontal SGS effect at the kilometer-scale resolution (Bryan and Rotunno 2009; Zhang et al. 2021b). Moreover, a tropical cyclone is warmest in its eye, and a substantial horizontal gradient of the equivalent potential temperature traverse the eyewall region (Houze 2014); therefore, the role of SGS turbulence might be even more important in the convection-permitting simulation of a tropical cyclone than in that of an ordinary convective storm in a different environment. Accordingly, evaluating such effects and potential methods to represent horizontal turbulence is the second goal of our study.

Here, we propose the use of a scale-aware cumulus parameterization and a new turbulence scheme to represent vertical and horizontal SGS mixing, respectively, in convection-permitting simulations. Section 2 describes the methods and characteristics of these schemes, and section 3 evaluates their performance in the case of a typhoon with a focus on predicting precipitation. Sections 4 and 5 investigate the physical processes that lead to improved simulations, and the final section summarizes our findings and discusses necessary further work.

2. Methods and experimental design

Our simulations were performed using version 4.2.1 of the Weather Research and Forecasting (WRF) Model (Skamarock et al. 2019) based on the case of Severe Typhoon Vicente (2012). We tested three different cumulus convection schemes that were switched on and off for the kilometer-scale inner domains in separate experiments for comparison. For the parameterization of horizontal turbulence, we compared various options, including not employing any scheme and using one of the two different SGS turbulence schemes. Below, we briefly describe the convection and turbulence schemes, after which we explain the configurations of our experiments.

a. *Cumulus parameterization*

The three cumulus convection schemes we used in our experiments are the Grell-3, Tiedtke, and multiscale Kain–Fritsch (MSKF) schemes, which correspond to options 5, 6, and 11, respectively, in the WRF Model; thus, we denote these schemes as C05, C06, and C11, respectively, to refer to the cumulus parameterizations in our experiments. Among these three schemes, the MSKF scheme is the only scale-aware parameterization intentionally designed to be used at both coarse and kilometer-scale resolutions. However, the other two schemes also have some characteristics that make them seemingly suitable for use in the gray zone, described below.

The Grell-3 scheme is based on the Grell–Devenyi ensemble scheme (Grell and Dévényi 2002), which is a mass-flux-type scheme that generates a large spread of variants by using numerous assumptions, including static control assumptions, such as updraft and downdraft entrainment and detrainment parameters and precipitation efficiency, and dynamic control assumptions, such as closure based on convective available potential energy (CAPE) or moisture convergence. The results from the abovementioned variants are averaged to give feedback to the resolved scales. The Grell-3 scheme modifies the Grell–Devenyi approach by eliminating ensemble members based on the quasi-equilibrium approach and by allowing subsidence to affect adjacent columns (Skamarock et al. 2019).

The Tiedtke scheme, which is also a mass-flux scheme, was modified from the original Tiedtke scheme (Tiedtke 1989) and implemented by Zhang et al. (2011). This scheme triggers convection when there is net moisture convergence, and the low-level air is buoyant when it rises to the lifting condensation level (Tiedtke 1989; Suhas and Zhang 2014). This scheme models shallow, midlevel, and deep convection; the strength of the latter two is determined by CAPE closure, while shallow

convection is maintained by the supply of moisture from surface evaporation. The parameterized shallow convection is more active in this modified Tiedtke scheme than in other schemes (Zhang et al. 2011), and thus, this scheme promotes the formation of boundary layer clouds. It is because of this characteristic that the modified Tiedtke scheme is a potential option for gray-zone simulations. Because the kilometer-scale resolution can arguably resolve deep convection but cannot effectively represent shallow convection because of its smaller scales (Pedruzo-Bagazgoitia et al. 2019). The modified Tiedtke scheme offers another attractive characteristic insomuch that the parameterized condensates detrained from the cloud top do not evaporate immediately; instead, these condensates are added to the clouds at the resolved scale.

The MSKF scheme was updated by Zheng et al. (2016) based on the widely used Kain–Fritsch scheme (Kain and Fritsch 1990, 1993; Kain 2004), which is a mass-flux parameterization with a trigger function based on the temperature perturbation related to the resolved-scale forcing. The original scheme has a CAPE closure and allows shallow convection, whereas in the updated MSKF scheme, the time scale for CAPE removal depends on the grid resolution; consequently, a finer grid mesh results in a longer time scale and thereby weaker tendency due to the parameterization, which helps the resolved convection dominate over the parameterized convection at fine resolutions. The minimum entrainment rate in the MSKF scheme is also scale-dependent and tends to increase as the resolution is refined, consistent with LES studies (Zheng et al. 2016). Furthermore, the MSKF scheme enhances resolved vertical velocities based on the SGS updraft mass fluxes.

It should be mentioned that WRF contains another scale-aware cumulus parameterization, the Grell–Freitas scheme (Grell and Freitas 2014). However, we included only one scale-aware scheme in our experiments to limit the total number of simulations and to keep the discussion concise.

b. *Horizontal turbulence parameterization*

Gradient-diffusion schemes, which can be computed by employing either an arbitrary constant diffusivity or the two-dimensional Smagorinsky model, are usually adopted to explicitly represent the effect of horizontal turbulence in WRF (Zhou et al. 2017). Accordingly, in this study, we evaluated the effects of implicitly representing horizontal turbulence (i.e., not using any parameterization and relying on numerical computations) and the effects of using two different parameterization schemes, namely, the Smagorinsky model and our newly developed reconstruction and nonlinear anisotropy (RNA) model.

The Smagorinsky model assumes SGS stress:

$$\tau_{ij} = -K_h D_{ij}, \tag{1}$$

where K_h is the horizontal eddy diffusivity, D_{ij} is the deformation tensor, and $i = 1, 2$ and $j = 1, 2$ indicate the horizontal directions. In WRF, linear interpolation might be needed due to the use of a C-grid, and another factor (not included above) related to the terrain-following coordinate needs to be applied (Skamarock et al. 2021). In WRF, horizontal diffusivity is determined by

$$K_h = C_s^2 l^2 \left[\frac{1}{4}(D_{11} - D_{22})^2 + D_{12}^2\right]^{1/2}, \tag{2}$$

where $C_s = 1/4$ and $l = (\Delta x \Delta y)^{1/2}$, with Δx and Δy being the horizontal grid spacings. The SGS scalar flux is calculated with equations of the scalar gradient and eddy diffusivity, similar to (1), and the scalar diffusivity is obtained by dividing K_h by the turbulent Prandtl number $\mathrm{Pr} = 1/3$.

The significant drawback of the Smagorinsky scheme is that it does not allow backscatter (upgradient flux), which is evidenced by in situ observations and LES results under some flow regimes (e.g., Carper and Porté-Agel 2004; Shi et al. 2018). Therefore, we developed a new turbulence scheme based on an explicit filtering framework that partitions the total turbulence flux into resolvable sub-filter-scale (RSFS) and SGS components (Chow et al. 2005). In other words, for the turbulence stress:

$$\tau_{ij} = \tau_{ij}^{\mathrm{RSFS}} + \tau_{ij}^{\mathrm{SGS}}. \tag{3}$$

Moreover, we adopt the idea of the dynamic reconstruction model (DRM) (Chow et al. 2005; Kirkil et al. 2012; Shi et al. 2018) and compute the RSFS component by reconstruction:

$$\tau_{ij}^{\mathrm{RSFS}} = \overline{u_i^* u_j^*} - \overline{u_i^*}\,\overline{u_j^*}, \tag{4}$$

where the overbar denotes a top-hat filter, the asterisk denotes reconstruction through deconvolution (for more details, see Chow et al. 2005; Shi et al. 2018), and u_i^* is simply the grid variable u_i for a zero-order reconstruction, which is adopted in this study for computational cost considerations.

The DRM uses a dynamic eddy diffusivity model for its SGS component and does not allow backscatter due to the numerical instability caused by a negative diffusivity coefficient. To overcome this drawback, we adopted the nonlinear backscatter and anisotropy (NBA) model (Kosović 1997; Mirocha et al. 2010) for the SGS component. The implementation of NBA in WRF can express the SGS stress in terms of either the strain rate alone or the SGS turbulent kinetic energy (TKE). We employ the strain-rate form of NBA to avoid additional ambiguity in computing TKE when we have the RSFS term. Therefore, the SGS stress in (3) is

$$\begin{aligned}\tau_{ij}^{\mathrm{SGS}} = {} & -C_s'^2 l^2 [2(2S_{mn}S_{mn})^{1/2} S_{ij} + C_1(S_{ik}S_{kj} - S_{mn}S_{mn}\delta_{ij}/3) \\ & + C_2(S_{ij}R_{kj} - R_{ik}S_{kj})],\end{aligned} \tag{5}$$

where $S_{ij} = D_{ij}/2$ is the resolved strain rate tensor, R_{ij} is the resolved rotation rate tensor, and δ_{ij} is the Kronecker delta. This function is based upon a reduced form of nonlinear constitutive relation and includes second-order terms, which account for backscatter and normal stresses. Details of the constants are documented in Mirocha et al. (2010). All constants eventually depend on a backscatter coefficient C_b, which accounts explicitly for backscatter. If $C_b = 0$, $C_1 = C_2 = 0$, and the terms

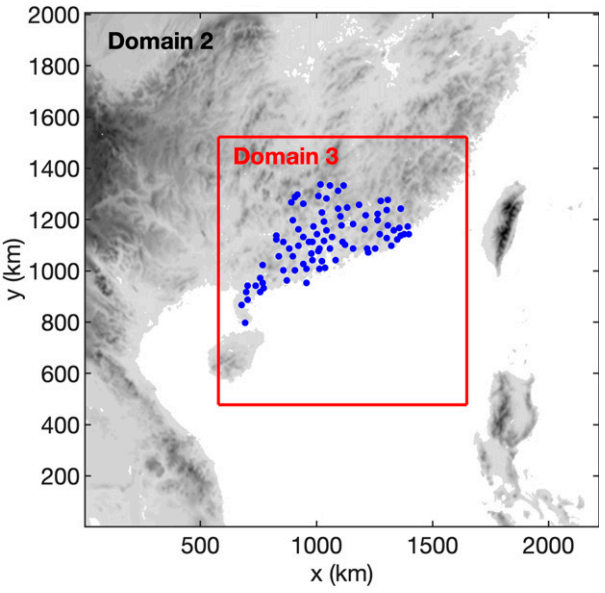

FIG. 1. Inner two domains of the WRF simulations. Domains 2 and 3 have grid spacings of 5 and 1.67 km, respectively. Gray shading indicates land, with darker colors representing higher surface elevations. Blue dots are the 86 surface stations in Guangdong Province whose data were used to evaluate the simulation performance.

responsible for backscatter, those in the brackets following C_1 and C_2, disappear.

Equations (3)–(5) constitute our new horizontal turbulence parameterization scheme, which is named the RNA model, which fully allows backscatter in the RSFS and SGS components. However, for scalar mixing, the NBA model does not provide a solution; hence, at present, the RNA model uses only the RSFS calculation (Shi et al. 2018) for scalar mixing.

c. Experiments

Our evaluation of the impacts of cumulus and turbulence parameterizations is based on WRF simulations of Severe Typhoon Vicente (2012). Typhoon Vicente made landfall at approximately 2000 UTC 23 July 2012, over Taishan in Guangdong, approximately 130 km to the west of Hong Kong (Hong Kong Observatory 2012). Our WRF simulation used three nested domains with grid spacings of 15, 5, and 1.67 km. Figure 1 shows the boundaries of the inner two domains. The simulations were initiated at 0000 UTC 23 July 2012, and were run for 48 h. The model output was archived every 30 min. The initial and lateral boundary conditions are based on the ECMWF fifth-generation reanalysis (ERA5) (Hersbach et al. 2020).

We conducted a series of simulations in which the cumulus and horizontal turbulence parameterizations are varied. Table 1 lists the simulations conducted in our study. In the outermost 15-km-resolution domain, the Smagorinsky scheme was always used for horizontal turbulence, and a cumulus convection scheme was always active, the choice of which was denoted "C*xx*" in the simulation name. When no cumulus or horizontal turbulence parameterization was used for domains 2 and 3, the simulation was marked as an "NC" simulation. When a cumulus convection scheme was used in the inner two domains, it was required to be the same option as the scheme used in the outermost domain. When a cumulus convection scheme was active in the inner domains, the choices of horizontal turbulence were denoted "CP," "CS," and "CR" in the experiment name to indicate no scheme, the Smagorinsky scheme, and the RNA model, respectively. Note that we did not conduct experiments in which the horizontal turbulence parameterization was used at the kilometer-scale resolution but no convection scheme is used at the same time because this configuration seems inconsistent with the assumption that the resolution of convective motions is in the gray zone. That is, if we assume convective motions are resolved, we should not use any parameterization, but if we assume they are under-resolved due to the gray zone, we should parameterize the subgrid effects in all three dimensions. Furthermore, we did not include a simulation that used the MSKF scheme for the outermost domain but had no convection scheme for the inner domains (C11-NC) because this configuration suffers from significant numerical instability and could not be completed.

TABLE 1. List of numerical experiments and the configurations of cumulus convection and horizontal turbulence schemes. Note that these options refer to the configurations in the two inner domains at the kilometer-scale resolution. The outermost domain always contains a cumulus parameterization and the Smagorinsky scheme for horizontal turbulence.

Expt	Convection scheme	Horizontal turbulence
C05-NC	None	None
C05-CP	Grell-3	None
C05-CS	Grell-3	Smagorinsky
C05-CR	Grell-3	RNA
C06-NC	None	None
C06-CP	Tiedtke	None
C06-CS	Tiedtke	Smagorinsky
C06-CR	Tiedtke	RNA
C11-CP	MSKF	None
C11-CS	MSKF	Smagorinsky
C11-CR	MSKF	RNA

The other numerical and physical schemes were identical among all the experiments. The simulation domains contained 50 vertical levels, and the model top was at 50 hPa. The three domains with different resolutions were two-way nested, allowing feedback from the high-resolution inner domains to their parent domains. The advection of momentum was computed using fifth- and third-order schemes for the horizontal and vertical directions, respectively, and the advection of moisture was implemented using a weighted essentially nonoscillatory (WENO) scheme. The cloud microphysics was computed with the Thompson scheme, which has been applied in previous tropical cyclone studies and exhibited high fidelity (Brown et al. 2016; Wu et al. 2021). Shortwave and longwave radiation were computed with the rapid radiative transfer model for global climate models (GCMs) (RRTMG).

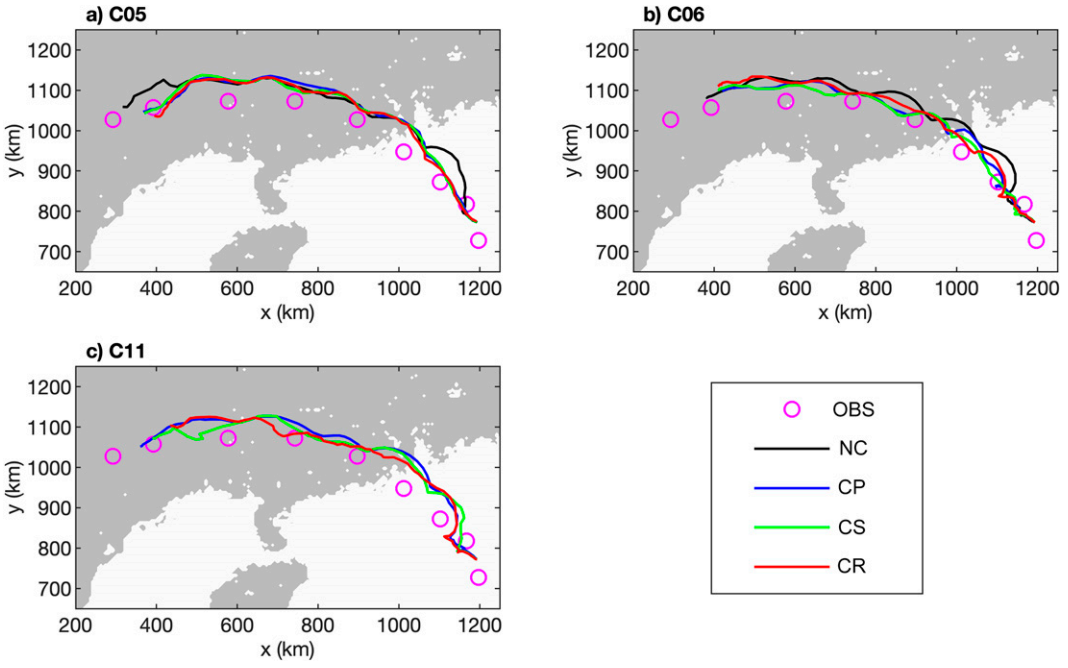

FIG. 2. Simulated tracks (solid lines) and observed best track (circles) of Typhoon Vicente. The best track data were obtained from CMA (2021) every 6 h. The initial position (0000 UTC 23 Jul 2012) is at the southeast corner of the plot. The typhoon moved northwest during the simulation period. The typhoon center is defined as the location with the minimum sea level pressure.

To model the effects of PBL processes, we used the scheme combining the quasi-normal scale elimination (QNSE) and eddy-diffusivity mass-flux (EDMF) schemes, namely, the QNSE-EDMF scheme. This scheme is chosen because EDMF is considered one potentially effective method to parameterize boundary layer turbulence in the gray zone (Chow et al. 2019). However, we also conducted supplementary test simulations in which QNSE-EDMF was replaced by the Yonsei University (YSU) PBL scheme. Metrics for simulation performance suggest qualitatively similar conclusions to what we described below in section 3 (see the appendix for details). Readers interested in the details of the aforementioned physical schemes are referred to Skamarock et al. (2021) and references therein.

Notably, we attempted to use a three-dimensional RNA scheme to replace the need for a PBL scheme in the inner domains. However, the resulting simulations substantially underestimated the intensity of Typhoon Vicente in terms of the surface pressure and precipitation at its center. We postulate that this underestimation occurred because, as mentioned earlier, the kilometer-scale resolution is, at best, within the margin of the gray zone for PBL turbulence. Moreover, the simulation of tropical cyclones is sensitive to vertical turbulence mixing in the PBL (Hill and Lackmann 2009; Rai and Pattnaik 2018). Because RNA is derived from schemes originally used in LES and relies more on resolved flow characteristics explicitly, it may significantly underestimate turbulent mixing within the PBL compared with a well-tuned conventional PBL scheme.

3. Simulation performance

In this section, we compare the results of the experiments listed in Table 1 against observations of Typhoon Vicente from various sources so that we can quantitatively judge the advantages and disadvantages of the different configurations and schemes.

The prediction of typhoon tracks by our simulations is evaluated in Fig. 2, in which the best track data from the China Meteorological Administration (CMA) (Lu et al. 2021; CMA 2021) are also plotted. The initial position of Typhoon Vicente is to the southeast of Hong Kong, whereas the starting positions of Typhoon Vicente in the simulations appear to be slightly north of the observed best track location due to errors in the ERA5. Nevertheless, all simulations appeared to produce similarly accurate tracks of the typhoon. The predicted tracks are slightly to the north of the best track but always within a distance of approximately 50 km. Likewise, the ending positions of the tropical cyclone center in the simulations are to the east of the observed best track location, but this error is observed to be relatively small in all simulations. Therefore, the short-term (48-h) prediction of typhoon tracks is not significantly influenced by our representation of unresolved convection and turbulence. This insensitivity is not surprising considering that the movement of a tropical cyclone is governed by a large-scale steering flow (Torn et al. 2018). Moreover, our simulations here to some extent benefited from the choice of initialization time. Approximately 12 h before our simulations' starting time, Vicente experienced a sudden northward track deflection, which is associated with the propagation

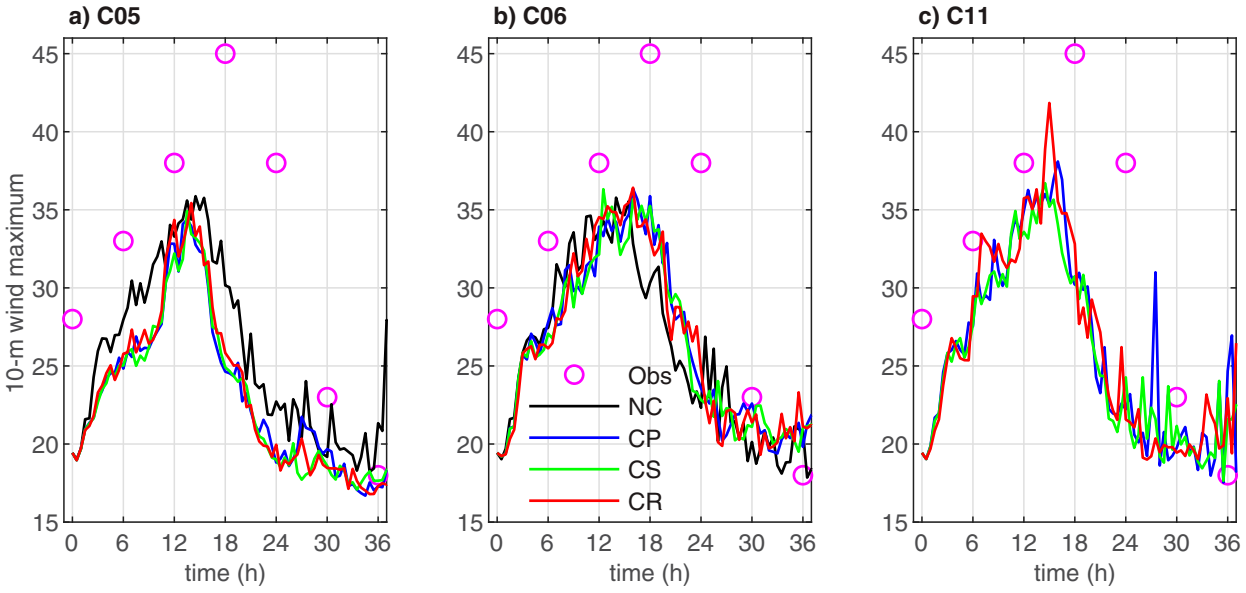

FIG. 3. Maximum sustained wind speed in the CAM best track data (Obs) and instantaneous maximum 10-m wind speed in WRF simulations. The best track data are available for every 6 h, and the WRF simulation data were archived every 30 min.

of an upper-level inverted trough and established northerly outflow channel associated with the inner-core reformation (Shieh et al. 2013; Chen et al. 2017).

Another challenge in the prediction of Vicente is its rapid intensification. Figure 3 shows the observed maximum 10-m wind speed from CMA best track data and that from WRF simulation data, which were archived every 30 min. The observation indicates that the maximum wind speed near the tropical cyclone center increases from 28 to 45 s^{-1} in 18 h. The WRF simulations started from a maximum wind speed of 19 s^{-1}, lower than observation. All simulations exhibit a rapid intensification with wind speed increases of at least 16 m s^{-1} in 18 h. However, among them, the maximum 10-m wind speed is between 34 and 36 m s^{-1} in the C05 and C06 group simulations, while in C11-CP, C11-CS, and C11-CR, the maximum near-surface wind speed is 38, 37, and 42 m s^{-1}, respectively. These results suggest that C11-CR tended to reproduce higher-intensity wind during Typhoon Vicente. In Fig. 3a, it is also clear that although those simulations using the Grell-3 cumulus scheme exhibit peak intensity similar to the C05-NC simulation without the cumulus parameterization, the intensity of the tropical cyclone before and after the peak is noticeably weaker in those than in the C05-NC simulation. This difference is consistent with the precipitation contrast in them described below. It should be noted that because our data were archived only every 30 min, there might be a slight underestimation of the maximum wind speed in all simulations (Nolan et al. 2014).

To evaluate the fidelity of the WRF simulations regarding the structure of Typhoon Vicente, we compare composite radar reflectivity in Fig. 4 for observation and simulations at approximately 1 h before Vicente's landfall in observation or each simulation. In the C05 and C06 groups, only the NC and CP simulations are included in the figure for conciseness. The radar observation (Fig. 4a) indicates that at its landfall, Vicente has a compact inner core and the diameter of its eyewall is approximately only 50 km. The tropical cyclone eyes in WRF simulations appear to have larger diameters. This error in eye size is especially larger for the simulations using the Grell-3 (C05-CP) and Tiedtke (C06-CP) cumulus schemes. The observed reflectivity exhibits banded spiral structures in which precipitation appears to be stronger in the eyewall region and in the rainbands. While simulations also exhibit banded structures, the rainbands in the simulations without cumulus parameterizations (C05-NC and C06-NC) are not so well organized and to some extent sporadic. The MSKF (C11) group of simulations exhibit more balanced performance in that they have relatively smaller eyes and continuous rainbands; and among those, C11-CR has the most compact inner-core structure. To quantify their size difference, we calculated the radius of maximum wind (RMW) with azimuthally averaged tangential wind at 850 hPa level and in the 3 h before landfall. The RMW values are denoted in brackets in the figure labels in Fig. 4. The C11-CR simulation exhibits the smallest RMW of 97 km, which is 20–30 km smaller than those of other simulations.

The prediction of precipitation is the main focus of our evaluation. To evaluate the prediction of the overall precipitation distribution, we used the accumulated precipitation from the 86 CMA surface stations in Guangdong Province (blue dots in Fig. 1) during the simulation period to calculate the spatial correlation coefficients between the simulated and observed accumulated precipitation (Fig. 5a) and the simulation bias in the average accumulated precipitation of the 86 stations (Fig. 5b). The simulation exhibiting the highest spatial correlation coefficient (0.58) with the observations is C05-NC, for which we did not employ any convection or horizontal turbulence schemes in the inner domains; however, its

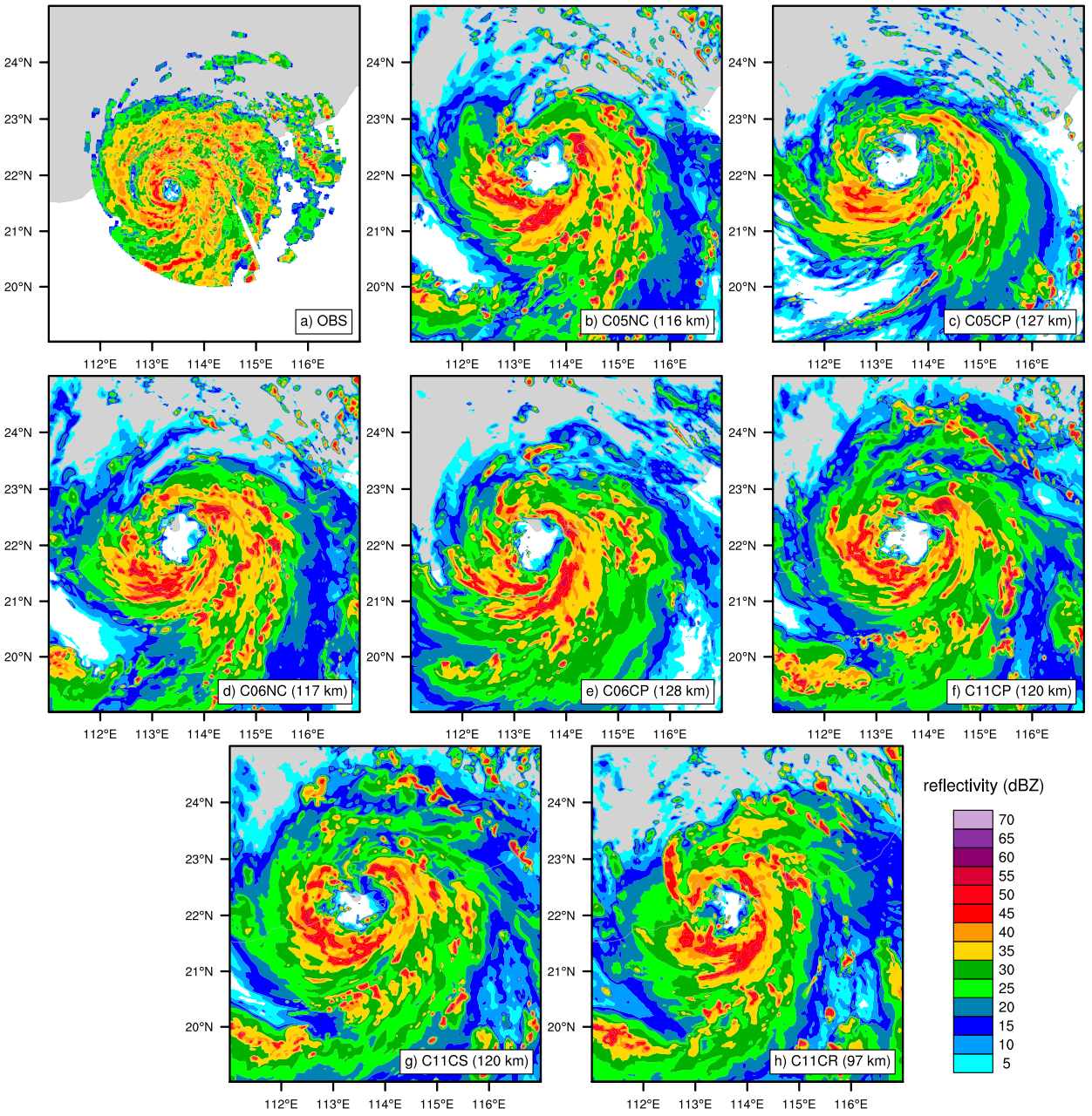

FIG. 4. Composite radar reflectivity in (a) observation and (b)–(h) in WRF simulations at 1 h before the landfall of the typhoon in observation or simulations. The observation is based on the Hong Kong Observatory's Doppler radar measurement. The values in parentheses following the panel labels are the radius of maximum wind (RMW), which is obtained by calculating the azimuthal-mean tangential circulation with the data from the 3 h preceding landfall and identifying the RMW at the 850-hPa level.

mean accumulated precipitation is approximately 14 mm less than the observed average of 83 mm. Switching on the convection scheme in the inner domains leads to a positive bias of 13–15 mm in the simulations (C05-CP, C05-CS, and C05-CR) and substantially lower spatial correlation coefficients of 0.39–0.45. For the simulations using the Tiedtke convection scheme (C06), the effect of the cumulus parameterization in the inner domains is similar: it helps avoid negative bias but lowers the spatial correlation coefficient by approximately 0.15. Thus, although C06-CP and C06-CR yield highly accurate mean precipitation predictions, considering their spatial details, their predictions are not better than those of the other simulations. The MSKF convection scheme (C11) group yields good spatial correlation coefficients (0.45–0.51), especially for experiments C11-CP and C11-CR. The experiment without any horizontal turbulence parameterization (C11-CP) displays a negative bias of approximately 7 mm, but adding a horizontal turbulence scheme ameliorates this problem. The bias of C11-CS is −4 mm, and that of C11-CR is +4 mm.

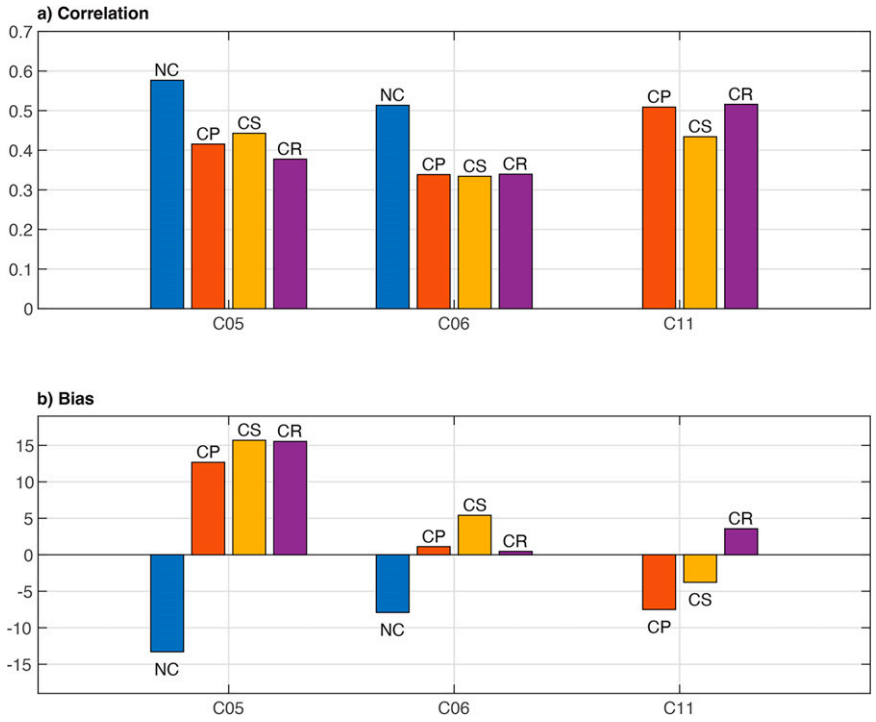

FIG. 5. (a) Spatial correlation coefficients between the accumulated precipitation amounts observed at the 86 stations in Guangdong Province (blue dots in Fig. 1) and those simulated by different WRF experiments. (b) Bias (mm) of the simulated mean precipitation at the 86 stations compared with the observations. The 86-station average of accumulated precipitation is 83.2 mm for the simulated 48-h period.

However, because C11-CS has a lower spatial correlation coefficient than C11-CR, the latter seems superior. Overall, C11-CR appears to perform better than the other experiments because of its balanced statistics, namely, a relatively high correlation coefficient and a small bias.

To further evaluate the capability of these simulations in predicting extreme rainfall events, we adopted the precision and recall metrics to measure each simulation's performance. Here, a station is said to observe an extreme event if its precipitation exceeds a given threshold. Precision is the fraction of the stations successfully predicted by a simulation to have experienced an extreme event (true positives) among all the stations predicted to have experienced extreme precipitation (true and false positives). In contrast, recall signifies the fraction of true-positive stations among all stations that experienced extreme events (true positives and false negatives).

Figure 6 plots the changes in precision and recall for the different experiments when the threshold of extreme precipitation is varied from 100 to 150 mm. Among the 86 stations, 26 stations recorded accumulated precipitation exceeding 100 mm during the 48-h period, and 15 stations recorded precipitation exceeding 150 mm. C05-NC exhibits the highest precision when the threshold is modest ($\leq$130 mm), but its recall rate is lower than most others, consistent with its negative bias in the average precipitation. Switching on the cumulus parameterization in the inner domains (C11-CP, C11-CS, and C11-CR) increases the simulation's recall but decreases the precision, meaning the simulations produce false alarms in addition to capturing actual extreme events. However, when the threshold exceeds 130 mm, precision and recall both drop substantially for the C05 group. In the C06 group, using or not using a convection scheme does not result in substantial differences in precision and recall when the threshold is less than 140 mm; again, however, precision and recall both drop as the threshold increases. For large thresholds (>140 mm), the C06 simulation not employing a cumulus parameterization in the inner domains (C06-NC) has significantly lower recall than the other simulations, including those in the C05 and C11 groups. The C11 group stands out because these simulations exhibit more significant differences among the simulations using different horizontal turbulence schemes than the C05 and C06 groups. When horizontal turbulence is modeled with the Smagorinsky scheme (C11-CS), precision and recall exhibit a dependency on the threshold similar to the simulations in the other groups; i.e., both decrease as the threshold increases. However, precision exhibits a loosely increasing trend in response to an increase in the threshold when neither a horizontal turbulence scheme nor the RNA model is used. Both C11-CP and C11-CR exhibit relatively high precision at large thresholds, with C11-CP being slightly superior. However, considering recall, C11-CR exhibits a substantial advantage. Therefore, if we focus on extreme precipitation with a large threshold, C11-CR appears to display the most balanced configuration, as it yields a relatively high precision and the best recall rate.

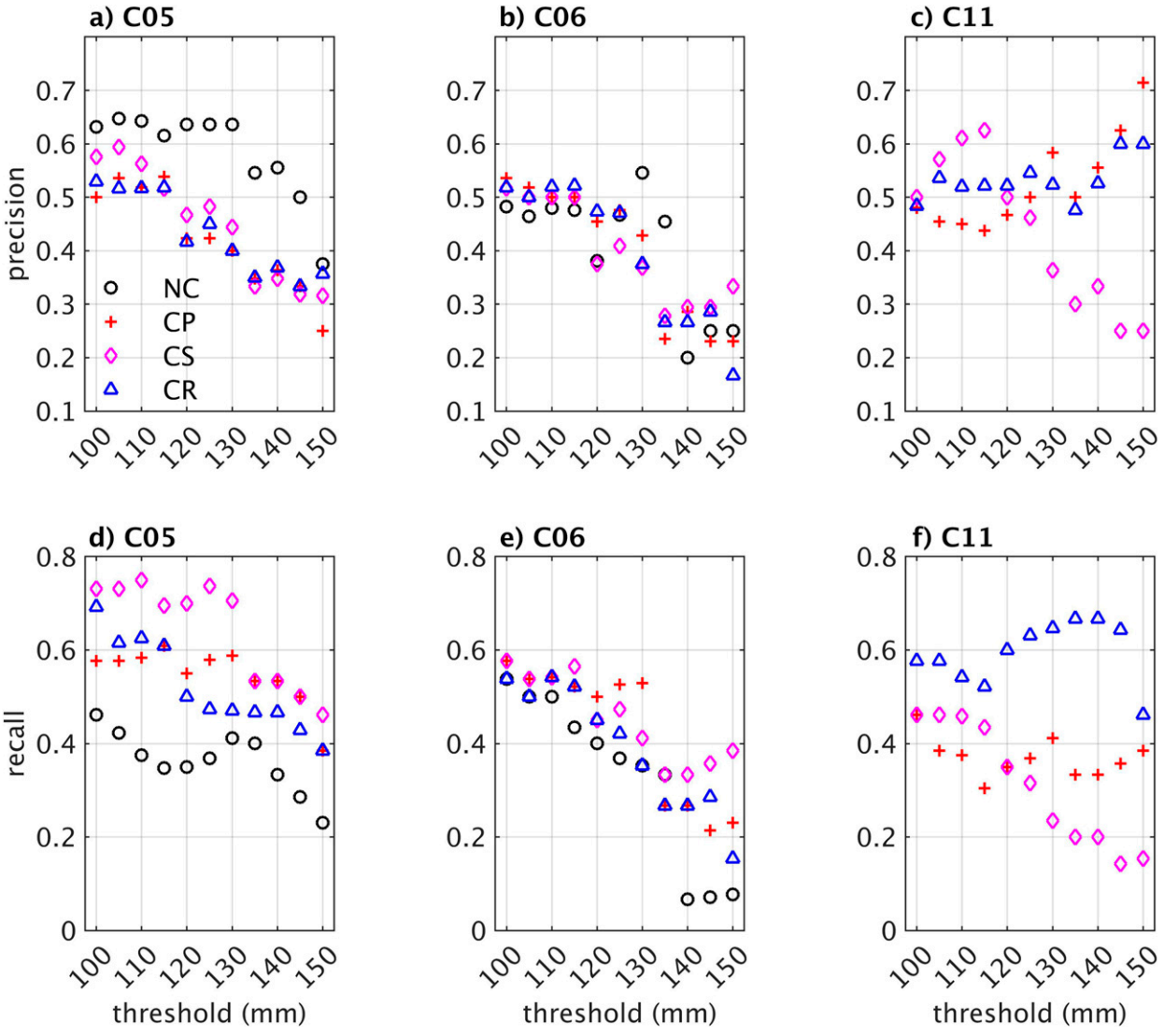

FIG. 6. (a)–(c) Precision and (d)–(f) recall of the numerical experiments as functions of the threshold for extreme precipitation. Precision is the ratio of the number of true positives to the summed number of true and false positives, while recall is the ratio of the number of true positives to the summed number of true positives and false negatives. Positive (negative) means the accumulated precipitation at a station is predicted by a simulation (not) to exceed the threshold. True or false refers to whether the observation is consistent with the prediction.

In summary, our evaluation in this section suggests that the Grell-3 and Tiedtke schemes might be unsuitable for kilometer-scale simulations of Typhoon Vicente. In contrast, the scale-aware MSKF scheme might be beneficial if combined with the newly developed RNA scheme for horizontal turbulence. The Grell-3 and Tiedtke schemes, when applied to the inner gray zone, increase the domain-average precipitation but decrease the spatial correlation coefficient; thus, the enhancement of precipitation may not be entirely physical. However, if no cumulus parameterization is used for the inner domains, the simulations suffer from underestimations of precipitation and therefore fail to predict extreme events (low recall), especially the events defined with high thresholds. For the MSKF scheme, the Smagorinsky and RNA schemes differ mainly in predicting extreme rainfall: when using relatively large thresholds to define extreme events, the Smagorinsky scheme undermines the prediction precision and recall, while the RNA scheme significantly enhances both metrics. Last, because here we only evaluated those schemes based on the Vicente case, it is necessary to admit that the robustness of the findings in this section needs to be further tested in future case studies.

4. Cumulus parameterization

To understand the effects of the cumulus parameterizations, we now focus on the simulations without using a horizontal turbulence scheme. Figure 7 shows the azimuthally

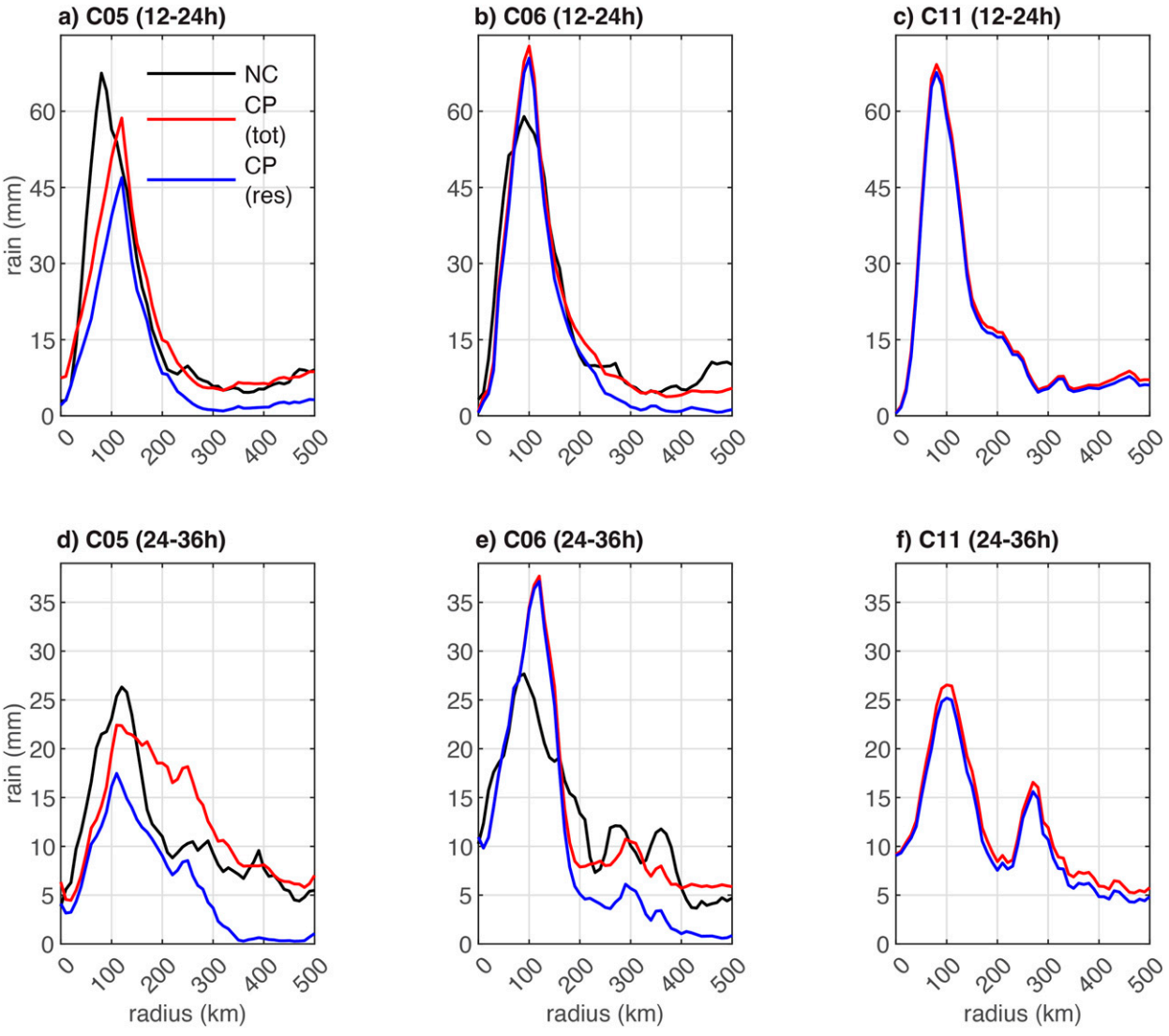

FIG. 7. Time-mean and azimuthal-mean precipitation as a function of the radius from the typhoon center, which is defined as the location with the minimum sea level pressure. The simulations without using a horizontal turbulence scheme in the inner domains (NC and CP) are shown. For the experiments using a convection scheme in the inner domains (CP), both the total (tot; red curves) and the resolved (res; blue curves) precipitation components are shown. Because the typhoon made landfall approximately at hour 20 of the simulations, (a)–(c) (averaged from hour 12 to hour 24), can be loosely defined as the pre-landfall average, and (d)–(f) (averaged from hour 24 to hour 36) represents the post-landfall average.

averaged precipitation in the simulations for two 12-h periods, loosely referred to as the pre-landfall and post-landfall periods. The different convection schemes appear to play considerably different roles in altering the precipitation. Using the Grell-3 scheme (C05) notably weakens the principal rainband, especially during the pre-landfall period. The parameterized precipitation contributes significantly to the total precipitation, especially in distant rainbands (200 km and farther from the center), where the resolved precipitation is very weak and the parameterized precipitation contributes the most to the total. During the post-landfall period, the convection scheme in the C05-CP experiment widens the principal rainband, and the parameterized precipitation extends the rainband far from the center; this effect seems to be the primary mechanism by which the negative domain-average bias becomes positive in Fig. 5. In contrast, the Tiedtke scheme (C06) enhances the principal rainband, which leads to the reduction of negative bias in the domain average; somewhat surprisingly, this enhancement is the result of an increase in the resolved precipitation. In distant rainbands, the effect of the Tiedtke scheme is similar to that of the Grell-3 scheme, i.e., replacing most of the resolved precipitation with parameterized rainfall in the distant rainbands. The different effects of the Grell-3 and Tiedtke scheme in the inner region are probably due to their different closure dependence. Grell-3 uses both moisture-convergence and CAPE-based closures, whereas the midlevel and deep

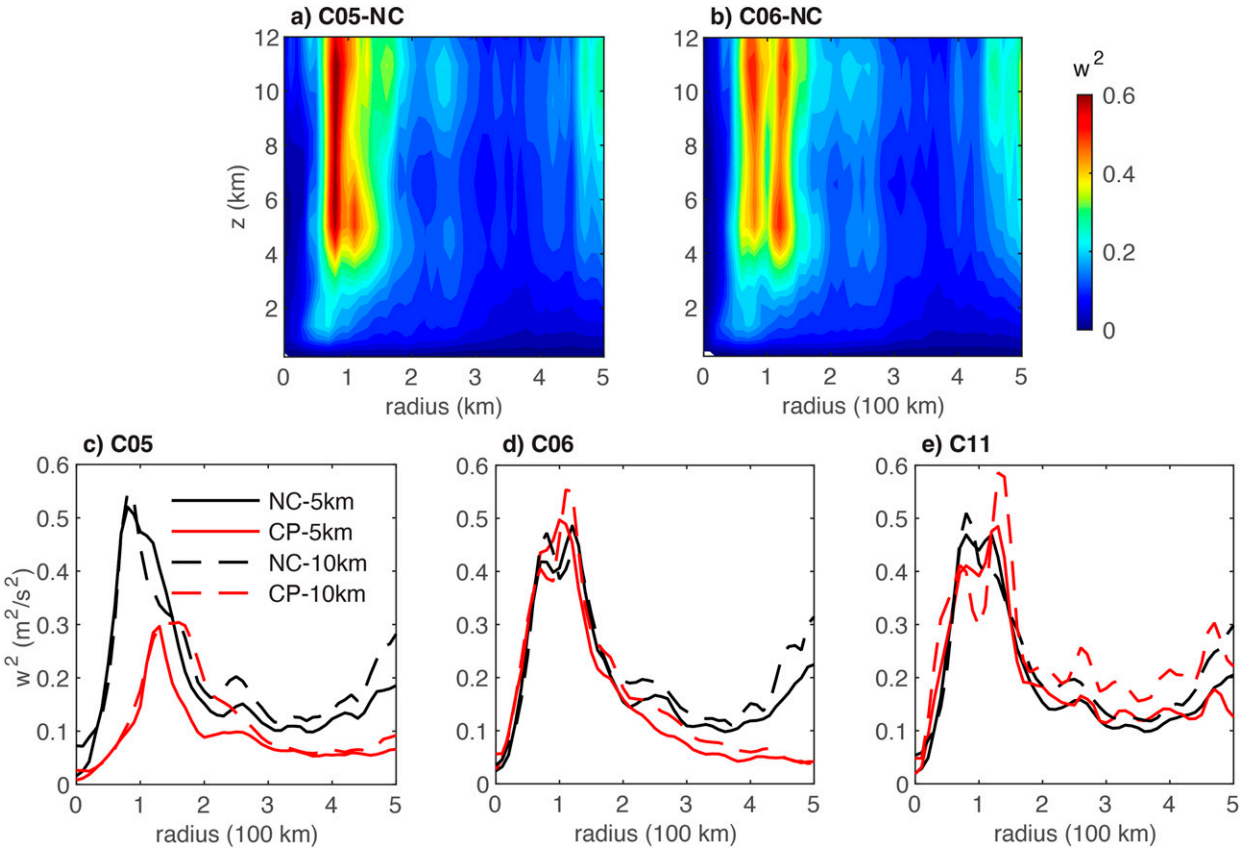

FIG. 8. Variance of the vertical velocity (w^2) in the simulations and the effects of a cumulus parameterization on it. (a),(b) The distributions of the time-mean and azimuthal-mean w^2 in the C05-NC and C06-NC simulations from hour 12 to hour 24. (c)–(e) The w variance at heights of 5 (solid lines) and 10 km (dashed lines) in the NC (black) and CP (red) simulations as a function of the radius from the typhoon center. In (e), the black curves are the means of the C05-NC and C06-NC results.

convection in the Tiedtke scheme is determined by CAPE only, which is relatively small near the inner core and large in the outer regions (Houze 2014).

The MSKF scheme's effect in C11-CP appears to be very gentle, probably due to its scale-dependent CAPE removal time scale. The precipitation distribution in C11-CP is close to the simulations that do not use a cumulus parameterization in the inner domains (C05-NC and C06-NC). During the pre-landfall period, the principal rainband precipitation peak is slightly higher than that in C05-NC and C06-NC, and during the post-landfall period, the principal rainband in C11-CP appears similar to those in the C05-NC and C06-NC simulations but with a secondary rainfall peak approximately 270 km from the tropical cyclone center. Notably, even in the distant rainbands of C11-CP, precipitation is dominated by resolved precipitation, and parameterized precipitation is minimal. Considering the lower bound of the gray zone resolution for deep convective cloud is 200–400 m (Shi et al. 2019), it is an interesting question to ask whether it is optimal tuning to make MSKF produce such little parameterized precipitation at the 1.67-km resolution. Further investigation in separate studies may be needed for this question.

The strength of the resolved convective motions is measured by the variance of the vertical velocity, which is plotted in Fig. 8. The effects of the cumulus parameterizations on convective motions are consistent with their effects on precipitation. In the C05 group, the cumulus convection parameterization substantially weakens the convective motions at the resolved scales for both the eyewall areas and the distant areas. The Tiedtke scheme in the C06 group weakens distant band convection but strengthens convective motions in the eyewall region, especially at the upper levels. The C11 group has no NC run for reference, but comparing the C11-CP results with the results averaged from C05-NC and C06-NC demonstrates that the MSKF scheme notably enhances the convective motions at the upper levels (Fig. 8e). Therefore, the effects of the Tiedtke and MSKF schemes are, to some extent, unexpected insomuch that a cumulus parameterization usually removes instability and therefore is expected to suppress the convective motions at the resolved scales, such as in the case of the Grell-3 scheme and the Tiedtke scheme for the outer regions, although the total precipitation might increase due to the contribution of parameterized precipitation.

To further understand how the Tiedtke and MSKF schemes may strengthen the resolved convection, we calculated the time-mean and azimuthal-mean parameterized convection scheme tendencies of the potential temperature and water vapor mixing ratio as functions of the radius from the typhoon

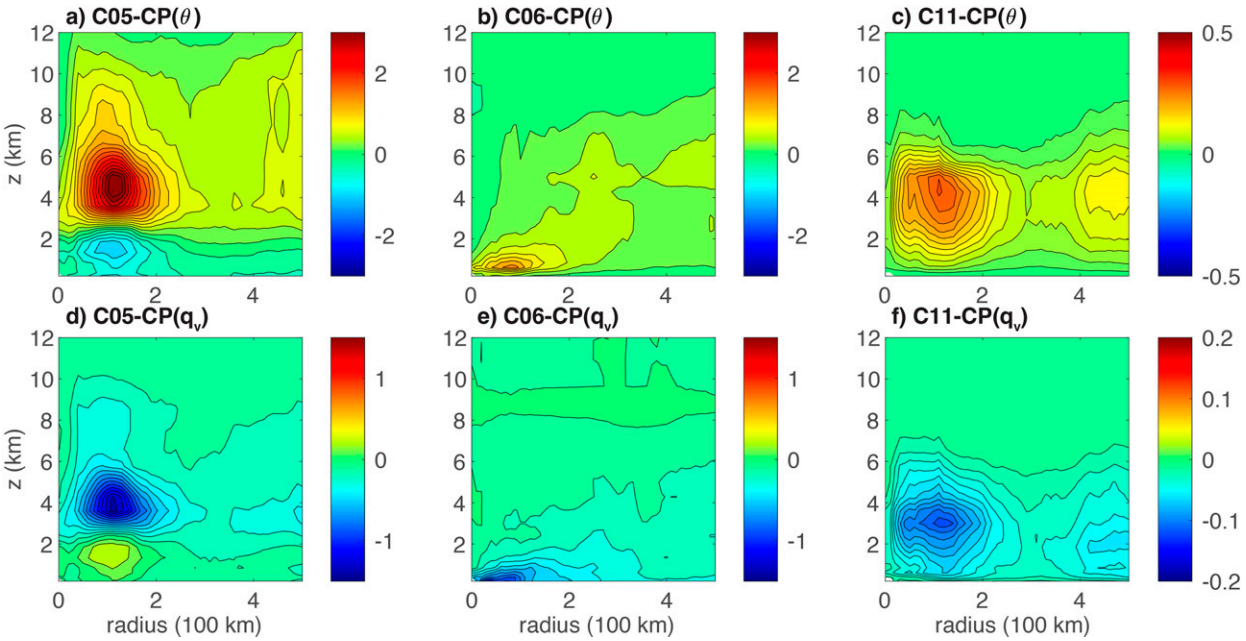

FIG. 9. Time-mean and azimuthal-mean tendencies of (a)–(c) the potential temperature (K h^{-1}) and (d)–(f) water vapor mixing ratio (g kg^{-1} h^{-1}) due to the cumulus convection parameterizations. These results are based on domain 3 data between hour 12 and hour 24 of the simulations. Note that (c) and (f) for C11-CP uses different color bars than (a), (b), (d), and (e).

center during the pre-landfall period (Fig. 9). In general, cumulus convection causes cooling and moistening through detrainment and triggers warming and drying in other regions by cumulus-induced subsidence (Arakawa and Schubert 1974). The Grell-3 scheme mainly appears to trigger deep convection; it cools and moistens the lower troposphere below 2.5 km and produces warming and drying tendencies at the levels above. Moreover, these tendencies are more substantial in the eyewall regions than in other places.

The Tiedtke scheme behaves differently in the eyewall region, where it produces primarily shallow convection (Figs. 9b,e). This convection dries and warms the boundary layer air, with a warming tendency slightly above the drying tendency. With regard to the buoyancy of air parcels, the warming effect substantially outweighs the effect of drying. Ascending air in the eyewall originates from the boundary layer. Therefore, the Tiedtke scheme's shallow convection parameterization appears to be the leading cause of its enhanced eyewall convection. In the outer regions, the Tiedtke scheme's parameterized convection is of intensity comparable to that of the Grell-3 scheme. However, because distant rainbands are only a relatively small fraction of the outer region area, the intensity of parameterized convection in the outer regions is not as intense as that in the inner regions for the Grell-3 and Tiedtke schemes.

The MSKF scheme triggers mainly deep convection, with the warming tendency reaching a maximum at a height of approximately 4 km and the drying tendency reaching a maximum at a slightly lower level. However, these tendencies are substantially weaker than (approximately only 1/5 of) those in the Grell-3 and Tiedtke schemes. Thus, the MSKF scheme weakly stabilizes the atmosphere, and this stabilization effect may not directly enhance the resolved convection.

However, different from the other schemes, the MSKF scheme also parameterizes SGS cloud–radiation interactions (Alapaty et al. 2012; Zheng et al. 2016). The cloud forcing calculations suggest that the C11-CP run indeed exhibits a larger cloud forcing near the center of the typhoon and in the outer regions (Fig. 10). Furthermore, the cloud forcing at the typhoon center is approximately 30 W m^{-2} stronger in the C11-CP simulation than in the other experiments shown in Fig. 10, whereas the C05-CP simulation exhibit a slight reduction in cloud forcing compared to its counterpart without a convection scheme. Alapaty et al. (2012) suggested that, in their simulations, the parameterized cloud–radiation feedback served to attenuate downward surface shortwave radiation and thereby reduced convective precipitation. Nevertheless, the cloud forcing here is primarily due to a change in longwave radiation and is therefore responsible for enhancing the convective motions through anomalous heating and the resulting positive moist static energy feedback. A recent study by Ruppert et al. (2020) highlighted the critical role of these feedbacks in accelerating tropical cyclone development and explained the detailed mechanisms.

5. Horizontal turbulence parameterization

As discussed in section 3, the advantages and disadvantages of the two horizontal turbulence parameterizations are not definite but are dependent on the cumulus parameterizations. The Smagorinsky scheme leads to more domain-average precipitation than the RNA model when they are combined with

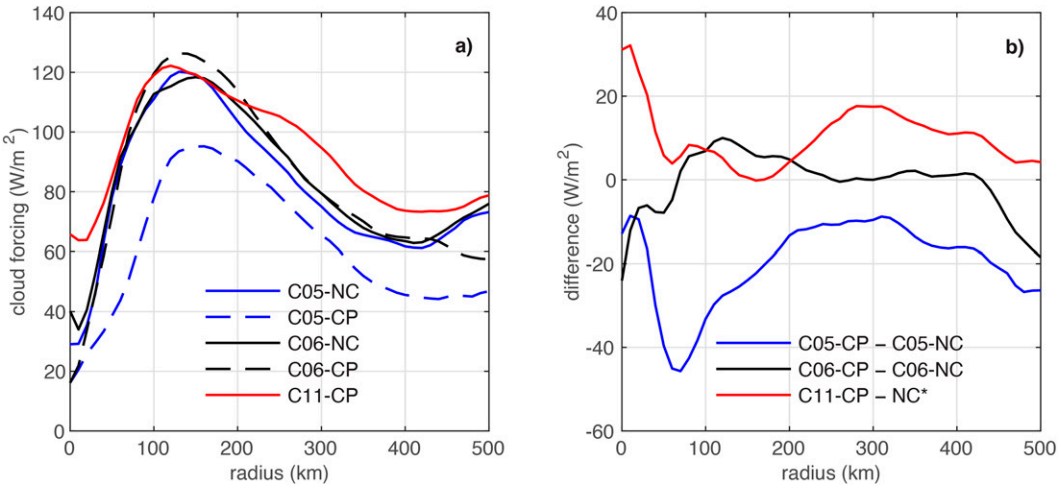

FIG. 10. (left) Cloud forcing in the simulations and (right) the difference among the simulations with and without the cumulus parameterization schemes. The cloud forcing here is defined as the change in net downward radiative flux (including longwave and shortwave radiation) at the top of the domain due to cloud feedback in the radiation calculation. In the right panel, NC* refers to the mean cloud forcing of C05-NC and C06-NC and is used to measure the cloud forcing change due to the MSKF scheme. These results are based on the domain 3 data between hour 12 and hour 24 of the simulations.

the Tiedtke scheme, but in comparison with the MSKF scheme, the RNA scheme results in more precipitation (Fig. 5). Figure 11 shows the simulated radial distributions of precipitation during the pre-landfall and post-landfall periods. The results are consistent with those depicted in Fig. 5. The exact reason for these differences is not known. However, we speculate that the cause is related to the patterns and strength of the parameterized cumulus convection tendencies. The Tiedtke scheme triggers mainly shallow convection in the eyewall region; thus, the horizontal turbulence parameterization, sensitive to wind shears [cf. Eqs. (1) and (5)], might actively interact with the convection scheme in the boundary layer and lower troposphere, where wind shears are strong. In contrast, the MSKF scheme causes gentler interference with the resolved flow, and its tendencies maximize in the middle troposphere; thus, the horizontal turbulence schemes may interact with the resolved flow rather independently.

Now, because C11-CR achieves the highest skill in predicting extreme precipitation events and the most balanced overall performance, we focus on the C11 group simulations. Figure 12 shows the strength of convective motions in each of the three C11 group simulations. The convection in the eyewall region is the most intense and widest in the CR experiment (Fig. 12c), while the CP experiment (Fig. 12b) exhibits narrower but more intense eyewall convection than the CS experiment (Fig. 12a). These characteristics are consistent with the precipitation in those simulations; i.e., the C11-CR simulation produces more precipitation overall and in the principal eyewall rainband, while C11-CP generates a higher eyewall maximum but less domain-average precipitation than C11-CS.

The differing convective activities result from the interaction between the parameterized turbulence and resolved flows. Whether a horizontal turbulence parameterization produces a downgradient or an upgradient can be measured by the product of the parameterized flux and gradients, which also indicates that the turbulence scheme causes the forward scattering or backscattering of energy (Shi et al. 2018). For the parameterized horizontal mixing of potential temperature (θ), the metric is

$$\Pi_\theta = -\tau_{\theta_j}\frac{\partial\theta}{\partial x_j}, \tag{6}$$

where $j = 1, 2$ indicates the horizontal directions and τ_{θ_j} is the parameterized horizontal turbulence flux of θ. Positive values of Π_θ indicate downgradient mixing (dissipation), whereas negative values indicate upgradient mixing (backscattering). A measure for moisture transport, Π_q, can be defined similarly with θ replaced by water vapor mixing ratio q in the above equation. For momentum, the metric is

$$\Pi = -\tau_{ij}\frac{\partial u_i}{\partial x_j}. \tag{7}$$

We can further split this metric Π into horizontal and vertical momentum components, Π_h and Π_v, respectively. Fr Π_h, $i = 1, 2$ and $j = 1, 2$; for Π_v, $i = 3$ and $j = 1, 2$. Again, positive and negative values indicate the downgradient and upgradient mixing of momentum, respectively.

We computed the above metrics for the RNA scheme in the pre-landfall period, and the results are shown in Fig. 13 as a function of the radius from the typhoon center together with the time-mean and azimuthal-mean tangential velocity and equivalent potential temperature as references. For the horizontal momentum (Fig. 13a), the RNA scheme produces upgradient mixing in the PBL and lower troposphere below

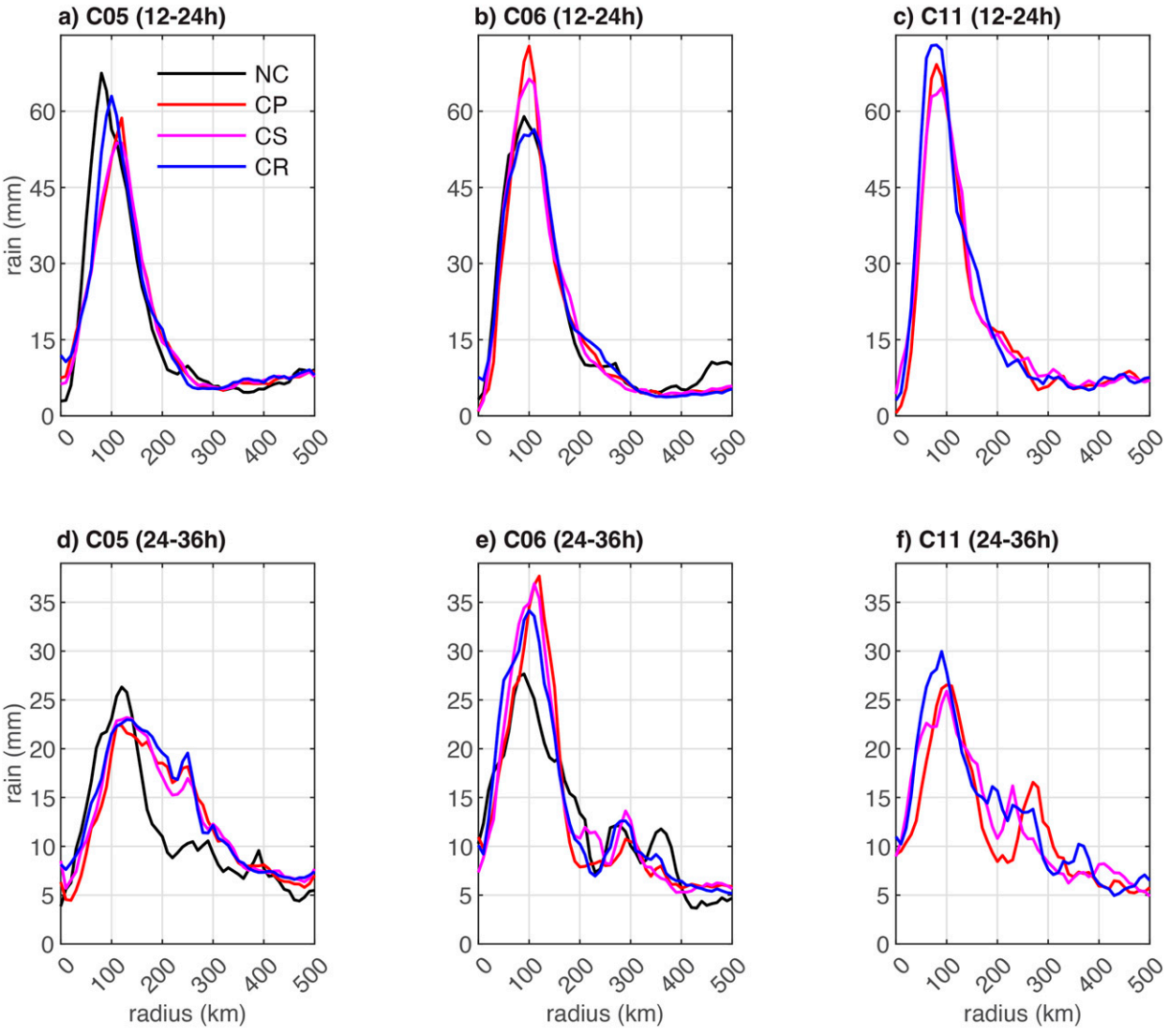

FIG. 11. Time-mean and azimuthal-mean precipitation during (a)–(c) the pre-landfall (hours 12–24) and (d)–(f) post-landfall (hours 24–36) periods as a function of the radius from the typhoon center.

2 km, above which height Π_h displays weak dissipation. Considering that the maximum tangential wind appears at approximately 1 km, the RNA scheme's main effect on the primary circulation is to enhance the low-level wind through backscattering. For the horizontal mixing of vertical velocities (Fig. 13b), RNA dissipates the kinetic energy associated with the vertical motions near the surface, but above approximately 1 km, Π_v is primarily negative. The upgradient transport of vertical momentum by the RNA scheme is especially strong in the center eye and eyewall region at heights between 1 and 2 km.

In the RNA model, the potential temperature (Fig. 13c) exhibits downgradient mixing in the PBL and lower troposphere; in the eyewall region, the downgradient mixing extends upward to a height of 4 km. In contrast, the upgradient transport of the potential temperature is most substantial in the upper troposphere of the eyewall. The low-level downgradient transport appears beneficial to transporting high-entropy air from the eye center outward and enhancing buoyancy of the upward motions in the eyewall; the upper-level backscattering also seems to help deepen convection due to its potential effect of reducing the entrainment of environmental air. The turbulence effect on moisture (Fig. 13d) is mostly backscatter in the boundary layer and lower troposphere, and the backscatter is especially strong in the tropical cyclone eye where dry air descends at the center. Thus, the overall effect of turbulence mixing on convection appears to be enhanced by reducing the entrainment of dry air into the convective cores at low levels.

Therefore, the horizontal turbulence effects parameterized by the RNA scheme invigorate convective motions in the typhoon primarily due to its optimal configuration of dissipation and backscatter. The upgradient transport of horizontal turbulence

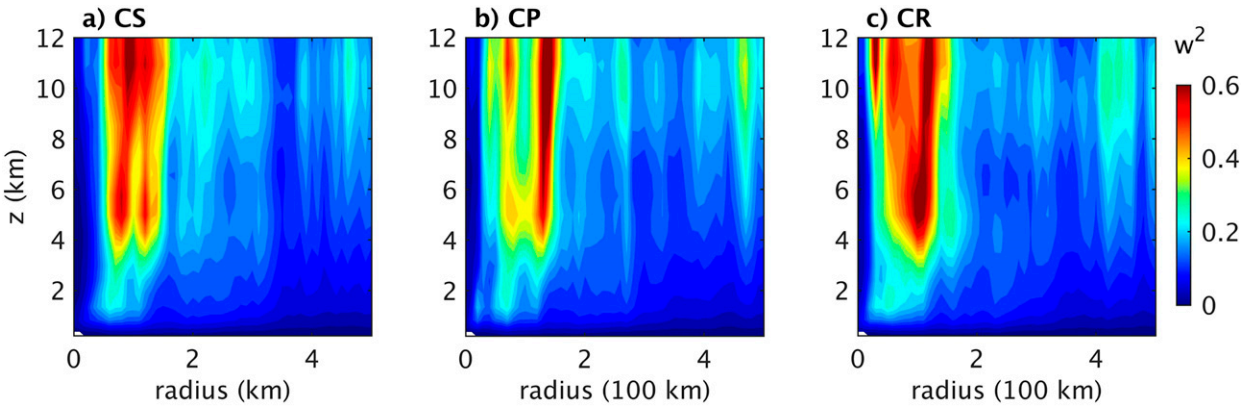

FIG. 12. The time-mean and azimuthal-mean variance of the vertical velocity (w^2) as a function of the radius from the typhoon center in the C11 (MSKF) group simulations: (a) C11-CS, (b) C11-CP, and (c) C11-CR. Simulation data from hour 12 to hour 24 are used.

enhances the tangential wind and thus the convective motion in the secondary circulation through dynamical adjustment. Moreover, the horizontal upgradient transport of vertical velocity in the troposphere is intense in the eyewall region, especially in the lower troposphere, thereby enhancing convection. The effects of the RNA scheme on buoyancy also favor more vigorous convection because the model enhances the low-level inflow buoyancy through horizontal downgradient mixing of heat and reduces entrainment through the upgradient mixing of moisture. It also reduces the upper-level dilution of updrafts with its upgradient transport of heat in the upper troposphere.

The location of momentum backscatter in Fig. 13 is consistent with previous flight and tower observations in tropical cyclones, which suggested that backscatter exists in the boundary layer of the inner-core region of a tropical cyclone and above the near-surface layer (Byrne and Zhang 2013; Tang et al. 2015). Examples of instantaneous distributions of

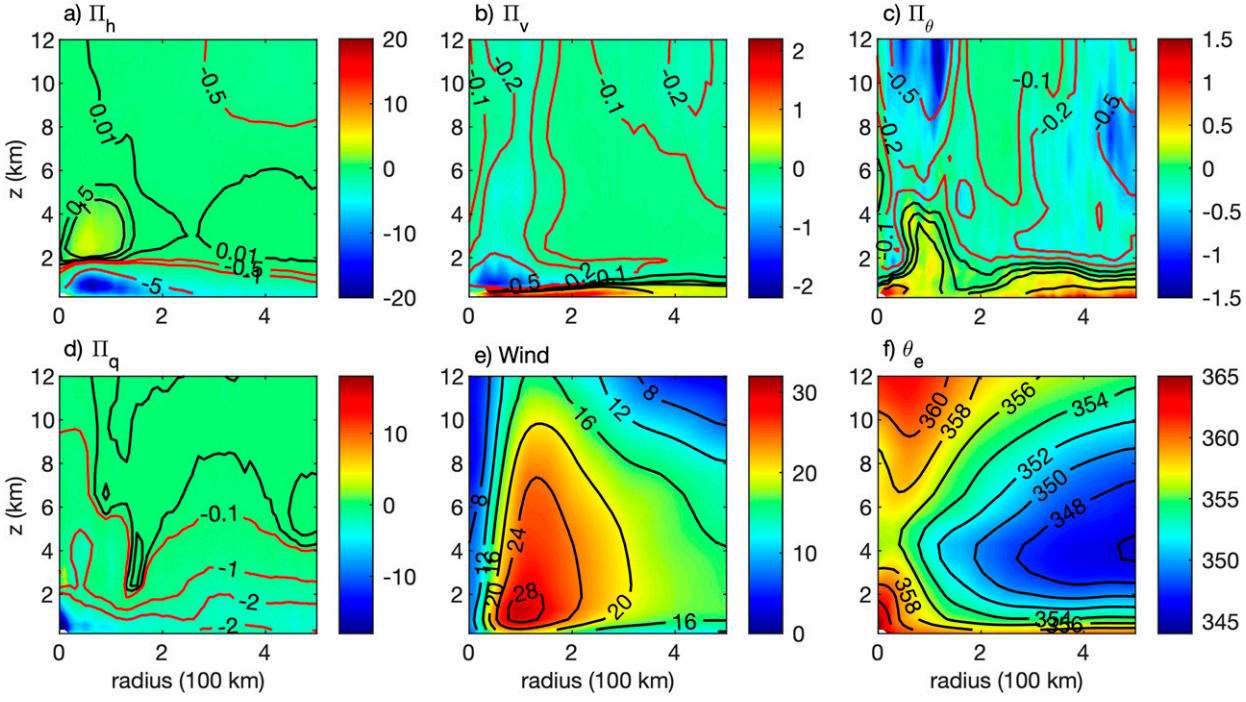

FIG. 13. Dissipation or backscatter of energy and scalar variance in the simulations due to the (a)–(d) RNA scheme-parameterized horizontal turbulence and are the (e) azimuthally averaged tangential wind and (f) equivalent potential temperature in the C11-CR simulation. (a) Dissipation (positive) or backscatter (negative) of the horizontal momentum (Π_h); red contours indicate negative values, while black contours indicate positive values (unit: $m^2\ s^{-2}\ h^{-1}$). (b) As in (a), but for the vertical velocity (Π_v). (c) Dissipation (positive) or backscatter (negative) of the variance of the potential temperature (unit: $K^2\ day^{-1}$). (d) As in (c), but for the water vapor mixing ratio (unit: $g^2\ kg^{-2}\ day^{-1}$). These results are based on the domain 3 data between hour 12 and hour 24 of the simulations.

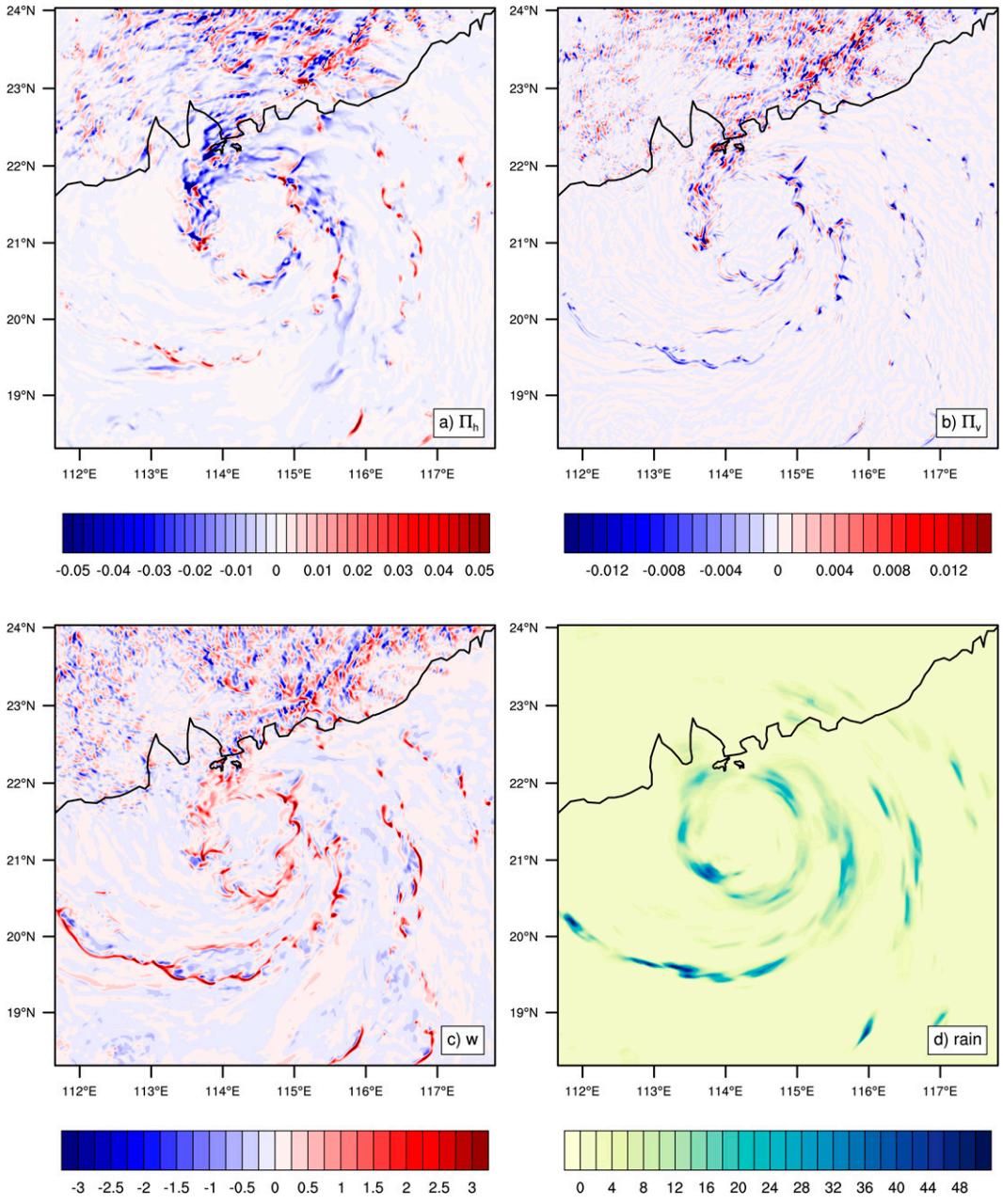

FIG. 14. Instantaneous distribution of (a) Π_h, (b) Π_v ($m^2\ s^{-3}$), and (c) vertical velocity, w ($m\ s^{-1}$), at the 925-hPa level at hour 12 of the C11-CR simulation; (d) the hourly precipitation (mm) ending at the same time.

Π_h and Π_v in the boundary layer are shown in Fig. 14, which also includes the vertical velocity and hourly precipitation. The upgradient transport of horizontal momentum by horizontal turbulence mixing mainly occurs near the eyewall rainband but extends outward for some distance. The upgradient transport of vertical momentum by horizontal turbulence mixing is mostly collocated with the eyewall and principal rainbands. The location difference in Figs. 14a and 14b is not surprising because gradients of horizontal and vertical velocities are distributed differently in a tropical cyclone. In both of them, forward-scatter is found next to the backscatter regions, but the area and intensity of the backscatter appear to be larger. Those features are qualitatively consistent with the finding of Sroka and Guimond (2021) using airborne radar observations of Hurricane Rita (2005). They suggest that the organization of backscatter is associated with coherent eddies, which affect the vortex dynamics through wave–wave nonlinear interactions and subsequently influence wave–mean flow interactions.

The characteristics of the Smagorinsky scheme are not shown here. This scheme can definitely produce only downgradient

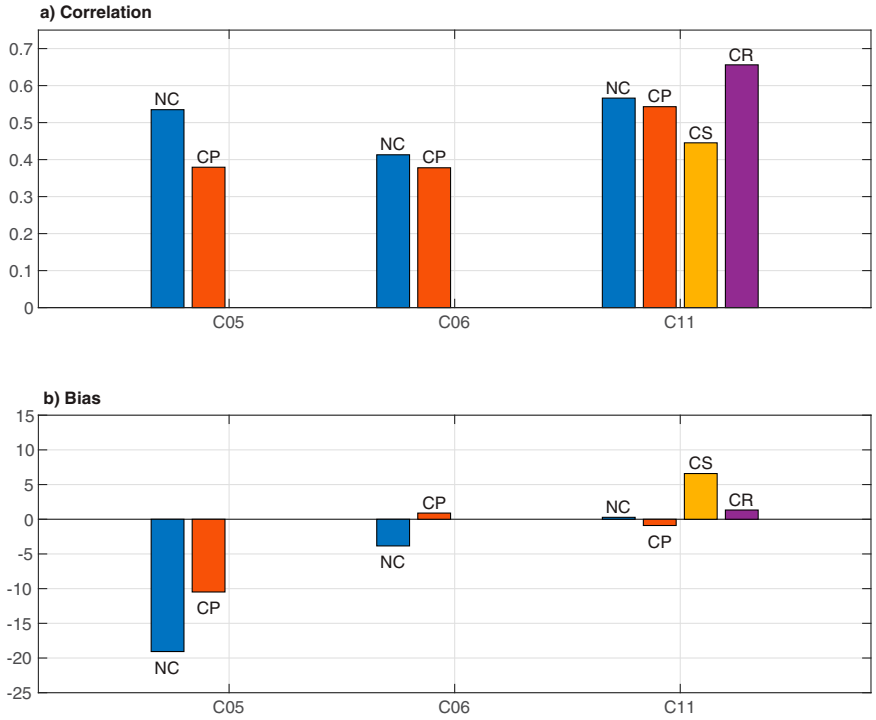

FIG. A1. As in Fig. 5, but that the simulations here used the Yonsei University (YSU) PBL scheme.

mixing everywhere. Thus, for momentum, the Smagorinsky scheme likely has the influence of diluting the maximum tangential wind in the primary circulation and the convective cores embedded in the secondary circulation. However, the downgradient mixing of buoyancy in the Smagorinsky scheme might facilitate eyewall convection because the center eye region possesses the highest entropy, and the Smagorinsky scheme can transfer entropy down along the gradient into the eyewall. The earlier evaluation in section 3 suggests that the C11-CS simulation achieves relatively low precision and recall when considering extreme precipitation events defined with a high threshold. Thus, the effects of the Smagorinsky scheme on the typhoon simulation are physically inappropriate.

6. Summary and discussion

The results of a recent a priori estimation of SGS fluxes based on the LES of a supercell case suggest that in gray-zone simulations of convection, SGS fluxes are comparable to resolved fluxes in magnitude and that vertical and horizontal SGS fluxes play equally important roles (Sun et al. 2021). Therefore, at kilometer-scale resolutions, it does not seem appropriate to simply switch off the cumulus and horizontal turbulence parameterizations and rely on the implicit diffusion of numerical schemes. However, conventional convection and turbulence schemes are designed for mesoscale modeling or LES with the corresponding assumptions, which become obsolete in gray zones. Thus, parameterizing the effects of SGS turbulence presents a conundrum for modelers.

In this study, we investigated the efficacy of various cumulus and turbulence parameterization schemes in improving the numerical prediction of a severe typhoon case. Our findings suggest that a viable path to gray zone parameterization for simulating convection is to represent the vertical and horizontal SGS effects separately using a scale-adaptive cumulus convection scheme for the former and a backscatter-enabled turbulence scheme for the latter. In our simulations, not using a cumulus convection scheme or a horizontal turbulence scheme at kilometer-scale resolutions results in the highest spatial correlation with the observed precipitation. However, the simulations suffer from underestimating the overall precipitation and achieve low scores in predicting rainfall extremes. When the Grell-3 and Tiedtke convection schemes are employed, the domain-average precipitation increases, but the spatial correlation drops significantly, suggesting that the modifications due to these schemes are not physically appropriate. The C11-CR simulation exhibits the best performance, as it achieves a reasonable spatial correlation coefficient, a small bias, and a high skill in predicting rainfall extremes. This simulation employs the MSKF scheme for vertical SGS convective motions and the RNA scheme for horizontal SGS turbulence in the inner domains with kilometer-scale resolutions.

Unlike the conventional schemes that introduce intruding tendencies into the simulations, the MSKF scheme generates relatively moderate tendencies, which dry and warm the lower to middle troposphere. However, this scheme enhances upper-level convective motions through its parameterization of the SGS cloud–radiation feedback, which is a mechanism different

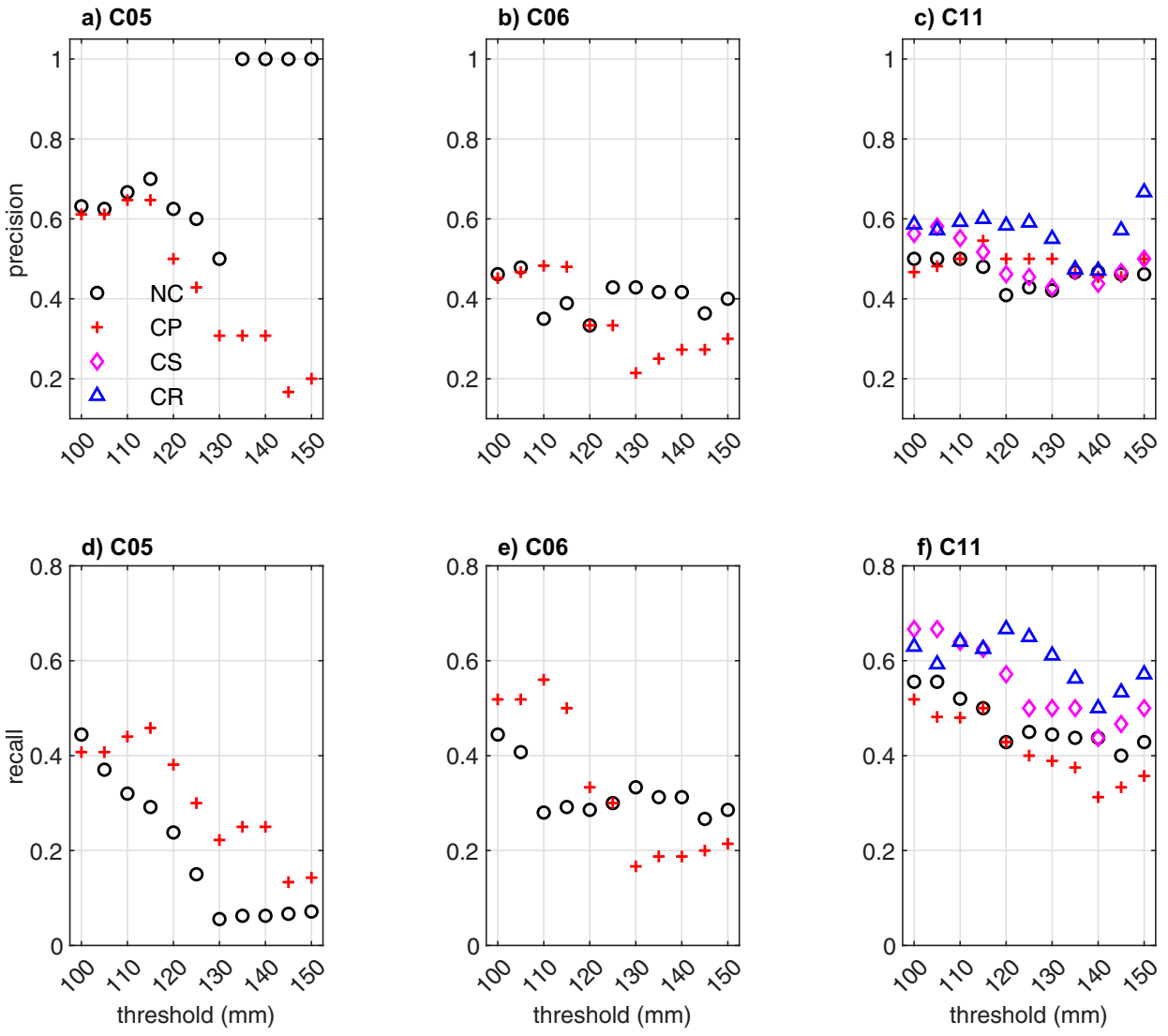

FIG. A2. As in Fig. 6, but that the simulations here used the Yonsei University (YSU) PBL scheme.

from the previous findings on how SGS convective mixing can benefit tropical cyclone intensification (Zhu et al. 2019; Chen and Bryan 2021). The RNA scheme further enhances the typhoon intensity and improves the prediction of rainfall extremes through its distribution of dissipation and backscatter. Furthermore, RNA generates the upgradient transport of momentum in the lower troposphere and thereby dynamically strengthens typhoon circulation. The RNA scheme displays mainly horizontal downgradient mixing of the potential temperature in the lower troposphere, so it helps enhance the buoyancy fed into the eyewall. In contrast, in the upper troposphere, the RNA scheme exhibits backscatter, thereby reducing the dilution of deep convective cores.

We used only a zero-order reconstruction in this study, as using a high-order reconstruction can significantly increase the computational cost. Nevertheless, the use of additional physical parameterizations certainly increases the computational cost. For instance, the MSKF scheme increases the computation time by approximately 8% compared to the simulations not using convection or horizontal turbulence schemes. Moreover, the use of the RNA scheme further increases the computation time by another 20%. These additional computational expenses of the proposed approach seem manageable and worthwhile considering the ongoing progress in computing power. However, because our evaluation is based on the Vicente case only, the robustness of the conclusions in other tropical cyclone cases remains to be investigated in future work.

Finally, we did not thoroughly investigate the configuration of the PBL turbulence parameterization. The conventional PBL schemes treat vertical mixing only. Thus, it is theoretically possible to combine a PBL scheme with the RNA model for parameterizing the horizontal directions. Previous studies suggested that the DRM may be suitable for gray-zone simulations

of cloud-topped boundary layers and ordinary convection (Shi et al. 2018, 2019). However, our tests (not shown) suggest that the typhoon intensity is substantially underestimated if we replace the PBL scheme with the three-dimensional RNA model. Thus, at least in the simulation of tropical cyclones, conventional PBL scheme formulations still have many advantages at kilometer-scale resolutions, although these advantages might not yet entirely extend into the gray zone for PBL turbulence. Nevertheless, the recent development of scale-aware PBL schemes (Shin and Hong 2015; Chen et al. 2021) provides yet another potential avenue for improving the gray-zone simulations of tropical cyclones.

Acknowledgments. The authors thank the three anonymous reviewers for their constructive comments and acknowledge Dr. Fotini Katopodes Chow and Dr. Jeffrey Mirocha for providing an earlier version of the DRM code implemented in WRF. This research was funded by the Research Grants Council of Hong Kong SAR, China (Projects HKUST-16301721 and AoE/E-603/18).

Data availability statement. The WRF Model code with the RNA parameterization can be found at https://doi.org/10.5281/zenodo.5880274, where the namelist files for all experiments are also included.

APPENDIX

Additional Tests with a Different PBL Scheme

To test the robustness of the conclusions in the main text, here we document additional test simulations using the Yonsei University (YSU) PBL scheme. The following figures (Figs. A1 and A2) suggest conclusions consistent with the main text. Specifically, the C05 (Grell-3) and C06 (Tiedtke) groups exhibit underestimation of domain accumulated precipitation if no convective cumulus scheme is used for the inner kilometer-scale-resolution domains; including the cumulus schemes in the inner domains ameliorate the low bias issue but lower the spatial correlation between simulated and observed precipitation patterns. The C11 (MSKF) group in general exhibits smaller biases and higher spatial correlation. The C11-CR simulation employing the MSKF and RNA scheme has the best performance for its small bias and highest correlation among all these runs. Figure A2 suggests the C11-CR simulation is most skillful in predicting extreme rainfall, because it exhibits higher precision and recall than other simulations, especially at high threshold rainfall amounts.

Recently, it has been suggested that using the Mellor–Yamada–Nakanishi–Niino (MYNN) PBL scheme might be beneficial to tropical cyclone simulations because of the inclusion of TKE advection (Chen and Bryan 2021). We indeed attempted to test the robustness of our results when adopting the MYNN scheme. However, the simulation combines RNA and MYNN suffers from numerical instability substantially. The conflicts between those two schemes are not known at present and are left for future investigations.

REFERENCES

Alapaty, K., J. A. Herwehe, T. L. Otte, C. G. Nolte, O. R. Bullock, M. S. Mallard, J. S. Kain, and J. Dudhia, 2012: Introducing subgrid-scale cloud feedbacks to radiation for regional meteorological and climate modeling. *Geophys. Res. Lett.*, **39**, L24809, https://doi.org/10.1029/2012GL054031.

Arakawa, A., and W. H. Schubert, 1974: Interaction of a cumulus cloud ensemble with the large-scale environment, Part I. *J. Atmos. Sci.*, **31**, 674–701, https://doi.org/10.1175/1520-0469(1974)031<0674:IOACCE>2.0.CO;2.

Boutle, I. A., J. E. J. Eyre, and A. P. Lock, 2014: Seamless stratocumulus simulation across the turbulent gray zone. *Mon. Wea. Rev.*, **142**, 1655–1668, https://doi.org/10.1175/MWR-D-13-00229.1.

Brown, B. R., M. M. Bell, and A. J. Frambach, 2016: Validation of simulated hurricane drop size distributions using polarimetric radar. *Geophys. Res. Lett.*, **43**, 910–917, https://doi.org/10.1002/2015GL067278.

Bryan, G. H., and R. Rotunno, 2009: The maximum intensity of tropical cyclones in axisymmetric numerical model simulations. *Mon. Wea. Rev.*, **137**, 1770–1789, https://doi.org/10.1175/2008MWR2709.1.

Byrne, D., and J. A. Zhang, 2013: Height-dependent transition from 3-D to 2-D turbulence in the hurricane boundary layer. *Geophys. Res. Lett.*, **40**, 1439–1442, https://doi.org/10.1002/grl.50335.

Carper, M. A., and F. Porté-Agel, 2004: The role of coherent structures in subfilter-scale dissipation of turbulence measured in the atmospheric surface layer. *J. Turbul.*, **5**, 040, https://10.1088/1468-5248/5/1/040.

Chen, X., and G. H. Bryan, 2021: Role of advection of parameterized turbulence kinetic energy in idealized tropical cyclone simulations. *J. Atmos. Sci.*, **78**, 3593–3611, https://doi.org/10.1175/JAS-D-21-0088.1.

——, Y. Wang, K. Zhao, and D. Wu, 2017: A numerical study on rapid intensification of Typhoon Vicente (2012) in the South China Sea. Part I: Verification of simulation, storm-scale evolution, and environmental contribution. *Mon. Wea. Rev.*, **145**, 877–898, https://doi.org/10.1175/MWR-D-16-0147.1.

——, M. Xue, B. Zhou, J. Fang, J. A. Zhang, and F. D. Marks, 2021: Effect of scale-aware planetary boundary layer schemes on tropical cyclone intensification and structural changes in the gray zone. *Mon. Wea. Rev.*, **149**, 2079–2095, https://doi.org/10.1175/MWR-D-20-0297.1.

Chow, F. K., R. L. Street, M. Xue, and J. H. Ferziger, 2005: Explicit filtering and reconstruction turbulence modeling for large-eddy simulation of neutral boundary layer flow. *J. Atmos. Sci.*, **62**, 2058–2077, https://doi.org/10.1175/JAS3456.1.

——, C. Schär, N. Ban, K. A. Lundquist, L. Schlemmer, and X. Shi, 2019: Crossing multiple gray zones in the transition from mesoscale to microscale simulation over complex terrain. *Atmosphere*, **10**, 274, https://doi.org/10.3390/atmos10050274.

CMA, 2021: China Meteorological Administration (CMA) tropical cyclone best track dataset. Accessed 22 September 2021, https://tcdata.typhoon.org.cn/.

Gao, Y., L. R. Leung, C. Zhao, and S. Hagos, 2017: Sensitivity of us summer precipitation to model resolution and convective parameterizations across gray zone resolutions. *J. Geophys. Res. Atmos.*, **122**, 2714–2733, https://doi.org/10.1002/2016JD025896.

Grell, G. A., and D. Dévényi, 2002: A generalized approach to parameterizing convection combining ensemble and data

assimilation techniques. *Geophys. Res. Lett.*, **29**, 1693, https://doi.org/10.1029/2002GL015311.

——, and S. R. Freitas, 2014: A scale and aerosol aware stochastic convective parameterization for weather and air quality modeling. *Atmos. Chem. Phys.*, **14**, 5233–5250, https://doi.org/10.5194/acp-14-5233-2014.

Hendricks, E. A., M. T. Montgomery, and C. A. Davis, 2004: The role of "vortical" hot towers in the formation of Tropical Cyclone Diana (1984). *J. Atmos. Sci.*, **61**, 1209–1232, https://doi.org/10.1175/1520-0469(2004)061<1209:TROVHT>2.0.CO;2.

Hersbach, H., and Coauthors, 2020: The ERA5 global reanalysis. *Quart. J. Roy. Meteor. Soc.*, **146**, 1999–2049, https://doi.org/10.1002/qj.3803.

Hill, K. A., and G. M. Lackmann, 2009: Analysis of idealized tropical cyclone simulations using the Weather Research and Forecasting model: Sensitivity to turbulence parameterization and grid spacing. *Mon. Wea. Rev.*, **137**, 745–765, https://doi.org/10.1175/2008MWR2220.1.

Hong Kong Observatory, 2012: Report on Severe Typhoon Vicente. Accessed 9 January 2022, https://www.hko.gov.hk/en/informtc/vicente/vicente.htm.

Honnert, R., and Coauthors, 2020: The atmospheric boundary layer and the "gray zone" of turbulence: A critical review. *J. Geophys. Res. Atmos.*, **125**, e2019JD030317, https://doi.org/10.1029/2019JD030317.

Houze, R. A., 2014: *Cloud Dynamics*. 2nd ed. Academic Press, 287–327.

Kain, J. S., 2004: The Kain–Fritsch convective parameterization: An update. *J. Appl. Meteor. Climatol.*, **43**, 170–181, https://doi.org/10.1175/1520-0450(2004)043<0170:TKCPAU>2.0.CO;2.

——, and J. M. Fritsch, 1990: A one-dimensional entraining/detraining plume model and its application in convective parameterization. *J. Atmos. Sci.*, **47**, 2784–2802, https://doi.org/10.1175/1520-0469(1990)047<2784:AODEPM>2.0.CO;2.

——, and ——, 1993: Convective parameterization for mesoscale models: The Kain–Fritsch scheme. *The Representation of Cumulus Convection in Numerical Models*, *Meteor. Monogr.*, No. 24, Amer. Meteor. Soc., 165–170.

Kendon, E. J., A. F. Prein, C. A. Senior, and A. Stirling, 2021: Challenges and outlook for convection-permitting climate modelling. *Philos. Trans. Roy. Soc.*, **A379**, 20190547, https://doi.org/10.1098/rsta.2019.0547.

Kirkil, G., J. Mirocha, E. Bou-Zeid, F. K. Chow, and B. Kosović, 2012: Implementation and evaluation of dynamic subfilter-scale stress models for large-eddy simulation using WRF. *Mon. Wea. Rev.*, **140**, 266–284, https://doi.org/10.1175/MWR-D-11-00037.1.

Kosović, B., 1997: Subgrid-scale modelling for the large-eddy simulation of high-Reynolds-number boundary layers. *J. Fluid Mech.*, **336**, 151–182, https://doi.org/10.1017/S0022112096004697.

Liu, C., and Coauthors, 2017: Continental-scale convection-permitting modeling of the current and future climate of North America. *Climate Dyn.*, **49**, 71–95, https://doi.org/10.1007/s00382-016-3327-9.

Lu, X., H. Yu, M. Ying, B. Zhao, S. Zhang, L. Lin, L. Bai, and R. Wan, 2021: Western North Pacific tropical cyclone database created by the China Meteorological Administration. *Adv. Atmos. Sci.*, **38**, 690–699, https://doi.org/10.1007/s00376-020-0211-7.

Mahoney, K. M., 2016: The representation of cumulus convection in high-resolution simulations of the 2013 Colorado Front Range flood. *Mon. Wea. Rev.*, **144**, 4265–4278, https://doi.org/10.1175/MWR-D-16-0211.1.

Mirocha, J. D., J. K. Lundquist, and B. Kosović, 2010: Implementation of a nonlinear subfilter turbulence stress model for large-eddy simulation in the advanced research WRF Model. *Mon. Wea. Rev.*, **138**, 4212–4228, https://doi.org/10.1175/2010MWR3286.1.

Nolan, D. S., J. A. Zhang, and E. W. Uhlhorn, 2014: On the limits of estimating the maximum wind speeds in hurricanes. *Mon. Wea. Rev.*, **142**, 2814–2837, https://doi.org/10.1175/MWR-D-13-00337.1.

Pedruzo-Bagazgoitia, X., P. A. Jiménez, J. Dudhia, and J. V.-G. de Arellano, 2019: Shallow cumulus representation and its interaction with radiation and surface at the convection gray zone. *Mon. Wea. Rev.*, **147**, 2467–2483, https://doi.org/10.1175/MWR-D-19-0030.1.

Porson, A. N., and Coauthors, 2020: Recent upgrades to the Met Office convective-scale ensemble: An hourly time-lagged 5-day ensemble. *Quart. J. Roy. Meteor. Soc.*, **146**, 3245–3265, https://doi.org/10.1002/qj.3844.

Rai, D., and S. Pattnaik, 2018: Sensitivity of tropical cyclone intensity and structure to planetary boundary layer parameterization. *Asia-Pac. J. Atmos. Sci.*, **54**, 473–488, https://doi.org/10.1007/s13143-018-0053-8.

Raynaud, L., and F. Bouttier, 2017: The impact of horizontal resolution and ensemble size for convective-scale probabilistic forecasts. *Quart. J. Roy. Meteor. Soc.*, **143**, 3037–3047, https://doi.org/10.1002/qj.3159.

Ruppert, J. H., A. A. Wing, X. Tang, and E. L. Duran, 2020: The critical role of cloud–infrared radiation feedback in tropical cyclone development. *Proc. Natl. Acad. Sci. USA*, **117**, 27 884–27 892, https://doi.org/10.1073/pnas.2013584117.

Seity, Y., P. Brousseau, S. Malardel, G. Hello, P. Bénard, F. Bouttier, C. Lac, and V. Masson, 2011: The AROME-France convective-scale operational model. *Mon. Wea. Rev.*, **139**, 976–991, https://doi.org/10.1175/2010MWR3425.1.

Shi, X., H. L. Hagen, F. K. Chow, G. H. Bryan, and R. L. Street, 2018: Large-eddy simulation of the stratocumulus-capped boundary layer with explicit filtering and reconstruction turbulence modeling. *J. Atmos. Sci.*, **75**, 611–637, https://doi.org/10.1175/JAS-D-17-0162.1.

——, F. K. Chow, R. L. Street, and G. H. Bryan, 2019: Key elements of turbulence closures for simulating deep convection at kilometer-scale resolution. *J. Adv. Model. Earth Syst.*, **11**, 818–838, https://doi.org/10.1029/2018MS001446.

Shieh, O. H., M. Fiorino, M. E. Kucas, and B. Wang, 2013: Extreme rapid intensification of Typhoon Vicente (2012) in the South China Sea. *Wea. Forecasting*, **28**, 1578–1587, https://doi.org/10.1175/WAF-D-13-00076.1.

Shin, H. H., and S.-Y. Hong, 2015: Representation of the subgrid-scale turbulent transport in convective boundary layers at gray-zone resolutions. *Mon. Wea. Rev.*, **143**, 250–271, https://doi.org/10.1175/MWR-D-14-00116.1.

Skamarock, W. C., and Coauthors, 2019: A description of the Advanced Research WRF version 4. NCAR Tech. Note NCAR/TN-556+STR, 145 pp., https://doi.org/10.5065/1dfh-6p97.

——, and Coauthors, 2021: A description of the Advanced Research WRF model version 4.3. NCAR Tech. Note NCAR/TN-556+STR, 165 pp., https://doi.org/10.5065/1dfh-6p97.

Sroka, S., and S. R. Guimond, 2021: Organized kinetic energy backscatter in the hurricane boundary layer from radar measurements. *J. Fluid Mech.*, **924**, A21, https://doi.org/10.1017/jfm.2021.632.

Suhas, E., and G. J. Zhang, 2014: Evaluation of trigger functions for convective parameterization schemes using observations.

J. Climate, **27**, 7647–7666, https://doi.org/10.1175/JCLI-D-13-00718.1.

Sun, S., B. Zhou, M. Xue, and K. Zhu, 2021: Scale-similarity subgrid-scale turbulence closure for supercell simulations at kilometer-scale resolutions: Comparison against a large-eddy simulation. *J. Atmos. Sci.*, **78**, 417–437, https://doi.org/10.1175/JAS-D-20-0187.1.

Tang, J., D. Byrne, J. A. Zhang, Y. Wang, X. Lei, D. Wu, P. Fang, and B. Zhao, 2015: Horizontal transition of turbulent cascade in the near-surface layer of tropical cyclones. *J. Atmos. Sci.*, **72**, 4915–4925, https://doi.org/10.1175/JAS-D-14-0373.1.

Tiedtke, M., 1989: A comprehensive mass flux scheme for cumulus parameterization in large-scale models. *Mon. Wea. Rev.*, **117**, 1779–1800, https://doi.org/10.1175/1520-0493(1989)117<1779:ACMFSF>2.0.CO;2.

Torn, R. D., T. J. Elless, P. P. Papin, and C. A. Davis, 2018: Tropical cyclone track sensitivity in deformation steering flow. *Mon. Wea. Rev.*, **146**, 3183–3201, https://doi.org/10.1175/MWR-D-18-0153.1.

Wu, D., F. Zhang, X. Chen, A. Ryzhkov, K. Zhao, M. R. Kumjian, X. Chen, and P.-W. Chan, 2021: Evaluation of microphysics schemes in tropical cyclones using polarimetric radar observations: Convective precipitation in an outer rainband. *Mon. Wea. Rev.*, **149**, 1055–1068, https://doi.org/10.1175/MWR-D-19-0378.1.

Wyngaard, J. C., 2004: Toward numerical modeling in the "terra incognita." *J. Atmos. Sci.*, **61**, 1816–1826, https://doi.org/10.1175/1520-0469(2004)061<1816:TNMITT>2.0.CO;2.

Zhang, C., Y. Wang, and K. Hamilton, 2011: Improved representation of boundary layer clouds over the southeast Pacific in ARW-WRF using a modified Tiedtke cumulus parameterization scheme. *Mon. Wea. Rev.*, **139**, 3489–3513, https://doi.org/10.1175/MWR-D-10-05091.1.

Zhang, X., J.-W. Bao, B. Chen, and W. Huang, 2021a: Evaluation and comparison of two deep convection parameterization schemes at convection-permitting resolution. *Mon. Wea. Rev.*, **149**, 3419–3432, https://doi.org/10.1175/MWR-D-21-0016.1.

——, B. Zhou, and F. Ping, 2021b: Effects of subgrid-scale horizontal turbulent mixing on a simulated convective storm at kilometer-scale resolutions. *Atmos. Res.*, **254**, 105445, https://doi.org/10.1016/j.atmosres.2020.105445.

Zheng, Y., K. Alapaty, J. A. Herwehe, A. D. Del Genio, and D. Niyogi, 2016: Improving high-resolution weather forecasts using the Weather Research and Forecasting (WRF) Model with an updated Kain–Fritsch scheme. *Mon. Wea. Rev.*, **144**, 833–860, https://doi.org/10.1175/MWR-D-15-0005.1.

Zhou, B., J. S. Simon, and F. K. Chow, 2014: The convective boundary layer in the terra incognita. *J. Atmos. Sci.*, **71**, 2545–2563, https://doi.org/10.1175/JAS-D-13-0356.1.

——, K. Zhu, and M. Xue, 2017: A physically based horizontal subgrid-scale turbulent mixing parameterization for the convective boundary layer. *J. Atmos. Sci.*, **74**, 2657–2674, https://doi.org/10.1175/JAS-D-16-0324.1.

Zhu, P., B. Tyner, J. A. Zhang, E. Aligo, S. Gopalakrishnan, F. D. Marks, A. Mehra, and V. Tallapragada, 2019: Role of eyewall and rainband eddy forcing in tropical cyclone intensification. *Atmos. Chem. Phys.*, **19**, 14 289–14 310, https://doi.org/10.5194/acp-19-14289-2019.